

NASA TECHNICAL NOTE



NASA TN D-2994

NASA TN D-2994



# EXPLORATORY EXPERIMENTAL AERODYNAMIC INVESTIGATION OF TENSION SHELL SHAPES AT MACH 7

*by James C. Robinson and Alfred W. Jordan*

*Langley Research Center*

*Langley Station, Hampton, Va.*

NATIONAL AERONAUTICS AND SPACE ADMINISTRATION • WASHINGTON, D. C. • SEPTEMBER 1965



TECH LIBRARY KAFB, NM



0130099

NASA TN D-2994

EXPLORATORY EXPERIMENTAL AERODYNAMIC INVESTIGATION  
OF TENSION SHELL SHAPES AT MACH 7

By James C. Robinson and Alfred W. Jordan

Langley Research Center  
Langley Station, Hampton, Va.

NATIONAL AERONAUTICS AND SPACE ADMINISTRATION

---

For sale by the Clearinghouse for Federal Scientific and Technical Information  
Springfield, Virginia 22151 - Price \$2.00

# EXPLORATORY EXPERIMENTAL AERODYNAMIC INVESTIGATION OF TENSION SHELL SHAPES AT MACH 7

By James C. Robinson and Alfred W. Jordan  
Langley Research Center

## SUMMARY

An exploratory experimental study of tension shell shapes for use in unmanned, planetary entry has been conducted. The tests were performed in the 7-inch (17.8-cm) Mach 7 pilot tunnel at the Langley Research Center at a stream stagnation temperature of approximately  $3420^{\circ}\text{R}$  ( $1900^{\circ}\text{K}$ ) and at Reynolds numbers ranging from  $0.043 \times 10^6$  to  $0.173 \times 10^6$ . The test medium was the combustion products of methane and air. The data collected were aerodynamic force and moment measurements, pressure distributions, and heating rates.

The investigation showed that some tension shell configurations deserve consideration for use as unmanned planetary-entry vehicles, as indicated by measured maximum drag coefficients of about 1.65. Flow separation from the surface of a tension shell shape was found to be the most important factor affecting its aerodynamic characteristics. The major significance of model length and nose bluntness was the effect on the extent of flow separation. Measured pitching-moment coefficients for the two relatively short models were slightly positive for nearly all angles of attack at which tests were made. The experimental pressure distributions obtained for these two models indicated that the assumption of a Newtonian pressure distribution is not valid. Heating studies showed that increasing the length of the tension shell configurations incurred attendant increases in the total convective heating rate if the flow remained attached to the body surface.

## INTRODUCTION

The use of atmospheric drag to dissipate most of the kinetic energy of an unmanned probe entering a thin planetary atmosphere such as that of Mars (discussed in refs. 1 and 2) will require a low value of the vehicle ballistic coefficient. Payload capability of the shapes heretofore considered for entry missions is small if the present minimum estimate of the density of the Martian atmosphere is considered.

An attempt to improve the payload capability of an entry vehicle resulted in the concept (presented in ref. 1) of a vehicle having a nose section containing the payload attached to a shell of revolution. This shell has negative Gaussian curvature and is supported at the base by a compression ring. (See fig. 1.) This design approach places the vehicle shell in tension and thereby attempts to optimize the structural weight while retaining a satisfactory drag coefficient. The theoretical development of this concept is presented in reference 3. Inasmuch as this approach attempts to optimize only structural weight, there are other parameters which are defined by aerodynamics that must be established in order to evaluate the applicability of this concept for use as an entry vehicle or hypersonic decelerator.

This paper presents the results of a preliminary investigation made to determine experimentally some of the aerodynamic parameters of shapes defined by this concept. Included in the results are drag coefficient, pressure distribution, flow-field characteristics, convective heating, and aerodynamic forces and moments. Inasmuch as very few data are available for this type of configuration, this investigation covered a broad range of shapes without intensive study of any one shape.

The tests were conducted in the 7-inch (17.8-cm) Mach 7 pilot tunnel at the Langley Research Center. The test medium was the combustion products of methane and air. The total energy of the test stream was about 1050 Btu/lbm (2440 kJ/kg). Free-stream total temperatures were about 3420° R (1900° K), and the Reynolds numbers based on model diameter ranged from  $0.043 \times 10^6$  to  $0.173 \times 10^6$ .

## SYMBOLS

The units used for the physical quantities in this paper are given both in the U. S. Customary Units and in the International System of Units (SI). Factors relating the two systems are given in reference 4 and those used in the present investigation are presented in the appendix.

$A_F$	maximum body frontal area, ft <sup>2</sup> (m <sup>2</sup> )
$A^2$	Newtonian shape parameter from reference 3
$c_p$	specific heat at constant pressure, Btu/lbm-°R (J/kg-°K)
$C_A$	axial-force coefficient, $\frac{-F_X}{q_\infty A_F}$ (see fig. 1)
$C_D$	drag-force coefficient, $\frac{F_D}{q_\infty A_F}$ (see fig. 1)

$C_N$	normal-force coefficient, $\frac{F_Z}{q_\infty A_F}$ (see fig. 1)
$C_m$	pitching-moment coefficient, $\frac{M_Y}{q_\infty A_F D}$ (see fig. 1)
$C_{p,s}$	stagnation-point pressure coefficient, $\frac{p_{t,2} - p_\infty}{q_\infty}$
$C_{\dot{Q}_c}$	total-convective-heating-rate coefficient, $\frac{\dot{Q}_c}{\rho V_\infty A_F H}$
$D$	diameter, ft (m)
$F_D$	drag force, lbf (N)
$F_X$	axial force, lbf (N)
$F_Z$	normal force, lbf (N)
$H$	total stream enthalpy, Btu/lbm (J/kg)
$l$	model reference length (see fig. 1), ft (m)
$M$	Mach number
$M_Y$	pitching moment about model moment center (see fig. 1), ft-lbf (m-N)
$p$	pressure, lbf/in. <sup>2</sup> (N/m <sup>2</sup> )
$\dot{Q}_c$	total convective heating rate, Btu/sec (J/s)
$\dot{q}$	local heating rate, Btu/sec-ft <sup>2</sup> (W/m <sup>2</sup> )
$q$	dynamic pressure, lbf/in. <sup>2</sup> (N/m <sup>2</sup> )
$r,x$	model coordinates, ft (m)
$r_b$	base radius perpendicular to model axis, ft (m)
$Re_D$	Reynolds number based on model maximum diameter, $\frac{\rho V_\infty D}{\mu}$
$R_n$	spherical radius of model nose, ft (m)
$t$	time, sec (s)
$T$	temperature, °R (°K)
$V$	velocity, ft/sec (m/s)

W	model mass, lbm (kg)
$\alpha$	angle of attack, deg
$\epsilon$	surface emissivity
$\mu$	absolute viscosity, lbm/ft-sec (N-s/m <sup>2</sup> )
$\rho$	stream density, lbm/ft <sup>3</sup> (kg/m <sup>3</sup> )
$\sigma$	Stefan-Boltzmann constant

Subscripts:

eq	radiation-equilibrium conditions
l	local conditions
R	denotes surroundings to which model radiates
t	stagnation conditions
w	wall
$\infty$	free stream
2	downstream of normal shock

## MODELS, APPARATUS, TESTS, AND PROCEDURES

### Models

Force models.- Axial forces were measured on twelve different basic model shapes. Two of these, designated models A and B, were tension shell shapes used for preliminary tests to determine whether the drag afforded by these shapes was adequately predicted by Newtonian theory. Seven were a family of tension shell shapes with ratios of length to base radius  $l/r_b$  varying from 0.6 to 3.0. This family was used in the systematic evaluation of the effect of body length and nose bluntness on aerodynamic drag. The three remaining were reference shapes - a 45° half-angle cone, a flat disk, and a typical blunt entry shape. All models tested had a maximum body diameter of 1.25 inches (3.18 cm).

Models A and B were machined from stainless steel and differed only in nose contour. Model B had a movable spike with a 5° half-angle conical nose with a small nose radius. The model coordinates and body geometry of models A and B are given in table I and figure 2.

The force models of the family of tension shell shapes and the reference shapes were machined from commercially pure copper. Copper was used because its high thermal conductivity would result in relatively low, uniform wall temperatures and

permit the use of the model as a calorimeter. Reference 5 indicated that relatively low wall temperatures are required to maintain flow attachment on similar shapes. The family of shapes and the  $45^\circ$  half-angle cone had ratios of nose radius to base radius ( $R_n/r_b$ ) that ranged from 0 to 0.40. The pertinent coordinates and geometric details for these models are presented in table II and figure 3.

The coordinates of the tension shell shapes, presented in tables I and II, were derived by using the method of reference 3 which assumes zero circumferential stresses when the shell is loaded with an axisymmetric Newtonian pressure distribution. The Newtonian shape parameter  $A^2$ , used in reference 3, was also included in these tables.

Pressure-distribution models.- Two pressure-distribution models were also fabricated from commercially pure copper. These models had a value of  $R_n/r_b$  near zero (approximately 0.025); one model had a length—base-radius ratio equal to 0.6 and the other model had a length—base-radius ratio of 0.8. (See fig. 4.) Each model contained ten 0.030-inch-diameter pressure orifices. One orifice was located at the stagnation point of the body. The remaining nine orifices were located at  $r/r_b$  from 0.2 to 0.9 in 0.1 intervals and were spaced radially about the models at  $30^\circ$  intervals except at  $r/r_b = 0.6$  where two orifices were placed  $180^\circ$  apart in order to indicate the symmetry of flow.

Heating-distribution models.- Fused-silica models fabricated by slip casting were used to make heating studies on two shapes with  $l/r_b$  values of 0.6 and 0.8 and a value of  $R_n/r_b$  of approximately zero. These silica models had the same external configuration and dimensions as the force models, with the exception that the support adapter was a stud cast in place during the model fabrication. The low thermal conductivity of this material assures that the external surfaces will rapidly approach radiation-equilibrium temperatures when subjected to aerodynamic heating. A more detailed description of the model fabrication may be found in reference 6. The use of such models for heating studies is discussed in more detail in the section entitled "Instrumentation."

### Apparatus

Tests were conducted in the 7-inch (17.8-cm) Mach 7 pilot tunnel at the Langley Research Center. This facility is a hypersonic blowdown tunnel with a high energy level obtained by burning a mixture of methane and air under high pressure, with the combustion products serving as the test medium for hypersonic flight simulation. Air is introduced at pressures up to 2300 psia ( $15.86 \text{ MN/m}^2$ ), mixed with the methane, and burned in a combustion chamber. The combustion products are then expanded through an axisymmetric nozzle and pass through a free-jet test section. (The properties of the combustion products can be found in ref. 7.) The flow is diffused in a straight-tube diffuser and pumped to atmosphere with a single-stage air ejector.

Tunnel stagnation temperatures are determined by recording the outputs of four platinum—platinum-13-percent-rhodium thermocouples located near the downstream end of the combustion chamber at various radial positions. The stagnation temperature is controlled by regulating the fuel-air ratio. Diametral surveys of pitot pressure and stagnation temperature for the length of the test region indicate a usable test-core diameter between 2.5 and 3.0 inches (6.3 and 7.6 cm). Over this diameter there is a  $\pm 2$ -percent variation in pitot pressure and total temperature (which corresponds to a maximum deviation of Mach number of  $\pm 0.07$ ).

For a given test, the flow in the tunnel is started and allowed to reach the desired equilibrium conditions. The model is then injected into the stream by means of a hydraulically actuated mechanism which requires approximately 1/4 second to position for testing. The model is removed from the test section after the desired interval and prior to tunnel shutdown.

The angle-of-attack system for the tunnel is hydraulically actuated and remotely controlled. The angle of attack can be either preset, in which case the model enters the stream at the preset angle, or a single specific angle can be attained while the model is in the stream. The system also has the capability of continuously moving the model through a range of angles of attack from  $-10^\circ$  to  $10^\circ$ , with the model rotation being controlled by throttling the hydraulic actuator. An offset sting or adapter is used to attain angles of attack larger than  $10^\circ$ . The actual angle of attack of the model, although preset for some cases, is checked by measurements from schlieren photographs.

### Instrumentation

Axial-force tests at zero angle of attack were made using a single-component (axial-force) strain-gage balance (fig. 5(a)). This balance was protected from the external stream by a shield fabricated from stainless steel and coated with aluminum oxide. Although the test durations were short, care was taken to determine that there was no change in zero-load output due to heating of the balance during the test.

The two models for which pitching-moment data were obtained were mounted on a six-component strain-gage balance (fig. 5(b)). Inasmuch as the bodies were axisymmetric and the yaw angle was maintained at zero, only three balance components (axial-force, normal-force, and pitching-moment) were used. The balance was protected from the external stream by a water-cooled heat shield made of stainless steel. An extension to the existing shield was fabricated from a thin sheet of copper. This extension was required to prevent heating of the balance caused by impingement of the external flow on the open end of the shield. (See fig. 5(b).) Water cooling of the front of the balance prevented heating due to conduction from the model.

Each copper force model was instrumented with one chromel-alumel thermocouple located at the juncture of the model support and the model base. (See fig. 3.) This thermocouple was used to indicate the total convective heating rate to the model when used on the single-component balance. Inasmuch as the thermal conductivity of copper is high, calculations showed that a single thermocouple would indicate satisfactorily, the mean-temperature-rise rate of the model. The thermocouple was installed in such a manner that it did not interfere with the force measurements.

Pressure measurements were obtained from the outputs of strain-gage-type pressure transducers. The pressure-distribution models remained in the stream until constant pressure readings were attained to assure proper response of the pressure pickups. In most cases, this time interval was approximately 5 seconds.

Radiation-equilibrium temperatures on the surface of the fused-silica heating-distribution models were recorded by a photographic pyrometer (ref. 8).

A single-pass schlieren system was used to obtain shock patterns around the models. Flash schlieren photographs were taken at  $1\frac{1}{2}$ -second intervals during the model test period with a flash duration of 4 microseconds.

### Tests

Tests of models A and B and the family of tension shell shapes were conducted at a Reynolds number of approximately  $0.08 \times 10^6$ . The corresponding tunnel stagnation pressure and temperature were about 1000 psia ( $6.89 \text{ MN/m}^2$ ) and  $3420^\circ \text{ R}$  ( $1900^\circ \text{ K}$ ), respectively. Axial-force measurements were obtained for model A at angles of attack from  $5^\circ$  to  $-5^\circ$  and for model B from  $10^\circ$  to  $-10^\circ$ . The models of the entire family of shapes were tested at zero angle of attack and at values of  $R_n/r_b$  from 0 to 0.40. Test durations were maintained at 6 to 10 seconds so that model temperatures normally did not exceed  $1000^\circ \text{ F}$  ( $811^\circ \text{ K}$ ).

The two shapes of the family with length—base-radius ratios of 0.6 and 0.8 and  $R_n/r_b = 0$  were tested at discrete angles of attack from  $0^\circ$  to  $20^\circ$  and at Reynolds numbers of  $0.043 \times 10^6$  and  $0.123 \times 10^6$ . Tests of the pressure-distribution models of these two shapes were conducted at several Reynolds numbers ranging from  $0.044 \times 10^6$  to  $0.171 \times 10^6$ . Heating-distribution models of these shapes were tested at a Reynolds number of  $0.09 \times 10^6$  with a test duration which exceeded 30 seconds.

During the tests, the outputs from the force balance, thermocouples, pressure pickups, and reference pressure transducers and thermocouples were recorded continuously. For data reduction and processing purposes, a significant portion of these outputs was also recorded simultaneously by the Langley central digital data recording facility.

## Data Reduction

Calculation of data coefficients.- The force data were reduced to conventional coefficients as defined in the symbol list.

For the solid-copper models, the rise in temperature with time at cold-wall conditions was determined by plotting  $\Delta T/\Delta t$  as a function of time by using the digital data record and extrapolating to zero time. A typical plot of model temperature and temperature gradient is shown in figure 6. The total convective heat-transfer rate was computed by using

$$\dot{Q}_c = Wc_p \left( \frac{\Delta T}{\Delta t} \right)_{\text{cold wall}}$$

The total heat input was assumed to be entirely convective inasmuch as the radiative-heat input was insignificant for the present test conditions. The calculated heating rate was then used to compute the total-convective-heating-rate coefficient  $C_{\dot{Q}_c}$  which is the fraction of the total energy of the approaching stream tube, as defined by the base of the body, that is absorbed as heat.

The heat-transfer distribution data were reduced by scanning the photographic image of the heated fused-silica model with a densitometer and determining the image density distribution over the model. The point readings were converted to temperatures by comparison with calibration data obtained from a known temperature source as described in reference 6. Equilibrium heat transfer could then be computed from radiation equilibrium as follows:

$$\dot{q}_{\text{eq}} = \epsilon \sigma (T_{w, \text{eq}}^4 - T_R^4)$$

where  $\epsilon$  is the total emissivity of the material. For the present test conditions,  $T_R^4$  was much smaller than  $T_{w, \text{eq}}^4$  and could be neglected.

Accuracy.- The estimated maximum experimental errors were as follows:

$C_D$ and $C_A$ . . . . .	±0.05
$C_N$ . . . . .	±0.02
$C_m$ . . . . .	±0.02
$C_{\dot{Q}_c}$ . . . . .	±0.003
$M_\infty$ . . . . .	±0.07
$p_l/p_{t,2}$ . . . . .	±0.03
$T_w/T_t$ . . . . .	±0.03
$\alpha$ , deg . . . . .	±0.10

In general it is believed that the probable errors in the faired data presented are less than the maximums indicated.

## RESULTS AND DISCUSSIONS

### Models A and B

The axial-force coefficients for model A along with schlieren photographs for the corresponding data points are presented as a function of angle of attack in figure 7. The axial-force coefficient at zero angle of attack is 1.12 and it increases to 1.51 at  $\alpha = -4\frac{1}{2}^{\circ}$ .

The axial-force coefficients obtained for model B are presented as a function of angle of attack in figure 8. At zero angle of attack, an axial-force coefficient of 1.66 was obtained for model B when the overall model length was set at 1.20 inches (3.05 cm). Excessive protrusion of the spiked nose resulted in loss of the high axial-force coefficient. A rapid decrease in the axial-force coefficient resulted as the angle of attack was varied from  $0^{\circ}$  to  $1^{\circ}$ ; however, as the angle of attack was increased beyond  $1^{\circ}$ , the value of  $C_A$  increased.

The axial force acting on a body in a flow is a function of the amount of flow compression afforded by the body. For given stream conditions, the amount of compression attained is dependent on the effective body shape, which is a function of both body geometry and boundary-layer growth and separation. Therefore, for the tension shell configurations, the existence of flow separation can have a decided effect on the axial-force coefficient. An examination of schlieren photographs of models A and B indicated that flow separation did exist under certain conditions. Model A had separated flow at zero angle of attack, and, as a result, the accompanying axial-force coefficient was comparatively small. As the model was pitched to an angle of attack, the flow attached on the windward side. This attachment resulted in a local increase in the compression and, hence, an increase in the overall axial-force coefficient. Model B also exhibited this dependence of axial-force coefficient on flow separation. At zero angle of attack the flow was attached, and a high axial-force coefficient resulted. Varying the spike protrusion had little effect on the axial-force coefficient as long as the flow remained attached. As the model experienced an increase in angle of attack from  $0^{\circ}$  to  $1^{\circ}$ , extensive flow separation occurred and the axial-force coefficient decreased sharply. Model B, as well as model A, exhibited a steady increase in axial-force coefficient with angle of attack beyond  $1^{\circ}$  as a result of the reduction in the extent of separation on the windward side of the body caused by the relieving effects of cross flow. It was therefore concluded that if flow separation from the surface of the tension shell shapes could be avoided, high values of the axial-force coefficient would result.

## Family of Shapes

The data from models A and B showed that relative body length could affect flow separation and, hence, the axial-force coefficient. Thus, an entire family of shapes with length—base-radius ratios varying from 0.6 to 3.0 was studied. Because sharply pointed bodies appear somewhat impractical as entry vehicles due to high aerodynamic heating of the nose, models with ratios of nose radius to base radius of 0 to 0.40 were also tested.

The results of the drag force measurements for the family of tension shell shapes at zero angle of attack are presented in figure 9. The corresponding schlieren photographs are presented as figure 10. Included in figure 9 are curves indicating the drag coefficients computed for the shapes with  $R_n/r_b = 0$  by using both Newtonian theory (as in ref. 3) and modified Newtonian theory. As shown in the figure, the shorter tension shell models afforded the higher drag coefficients with a maximum of about 1.65. The experimental drag coefficients for these shapes exceeded the Newtonian values. This lack of agreement was due primarily to the fact that flow separation was avoided for these shapes (see fig. 10), and some centrifugal effects with attendant higher pressure recovery on the skirt of the bodies was obtained. Figure 10 also indicates that the flow separation increased with model length until little of the geometric shape was effective. The effective body shape resulting from separation was approximately a cone which decreased in apex angle as the body length increased. Consequently, the drag coefficient decreased with increased body length. It is therefore clear that the drag of such tension shell shapes is critically dependent on flow separation.

It is further indicated in figure 9 that the drag coefficient decreased with increasing nose bluntness, probably because the spherical nose of the bodies promoted flow separation from the model surface. Nose bluntness had little effect on the drag of the short models but became more important as model length increased. As nose radius was increased, the drag coefficient reached a minimum, and then began to increase. This increase resulted from the fact that the drag of the blunt nose became large enough to increase the drag coefficient.

For comparative purposes the drag coefficients of the flat disk, the typical blunt entry body, and the  $45^\circ$  half-angle cone are also plotted in figure 9. It is observed that the drag coefficients for the shorter members of the family of shapes slightly exceeded that for the flat disk and were considerably higher than that for the blunt entry body. An examination of the schlieren photographs (fig. 10) for the entire family of tension shell shapes resulted in the same conclusion as that reached for models A and B; that is, if attached flow is maintained over the body, high drag will result.

The convective heating-rate coefficients obtained are shown in figure 11. The total convective-heat input was a maximum at a value of  $l/r_b$  of approximately 1.0. An increase in flow separation as  $l/r_b$  increased above 1.0 resulted in a corresponding decrease in total convective heating. A presentation of the ratio of the convective heating-rate coefficient to the corresponding drag coefficient ( $C_{\dot{Q}_c}/C_D$ ) shows that the short models afforded the highest drag for the least amount of convective-heat input (fig. 12). Low values of this ratio appear desirable for entry vehicles inasmuch as heat-protection weight might comprise a large portion of the total vehicle weight.

#### Aerodynamic Force Data at Angles of Attack

Tests to determine aerodynamic coefficients for two of the models ( $l/r_b = 0.6$  and  $0.8$ ;  $R_n/r_b = 0$ ) which exhibited high drag coefficients were conducted at angles of attack from  $0^\circ$  to  $20^\circ$ . The results are presented in figure 13 for Reynolds numbers of  $0.043 \times 10^6$  and  $0.123 \times 10^6$ ; the corresponding schlieren photographs are shown in figure 14. For both values of  $l/r_b$ , the axial-force coefficients increased slightly with angle of attack to a point between  $3^\circ$  and  $5^\circ$  and then began to decrease. At  $\alpha = 20^\circ$  the axial-force coefficients were approximately 85 percent of the values at  $\alpha = 0^\circ$ . Figure 13 indicates that for the relatively short configurations a comparatively high value of axial-force coefficient is maintained at angles of attack other than zero and also the effect of the Reynolds number is small. These results are due to the fact that no significant flow separation occurs for these shapes in this angle-of-attack or Reynolds number range.

The pitching-moment coefficient  $C_m$  was slightly positive about the model moment center for nearly all angles of attack at which tests were made. The pitching moments and the corresponding normal forces indicate a lack of static stability for center-of-gravity locations near the model half-length location. It should be noted that misalignment of the model axis with the balance axis might have caused errors in the absolute values of  $C_m$ . However, the relative magnitudes of the pitching-moment coefficients are so small that for any center-of-gravity location between the nose of the model and the base, the two models have, at best, only marginal static stability at small angles of attack. The results of reference 9 indicate that longer models ( $l/r_b \approx 1.4$ ) may exhibit positive static stability.

#### Pressure Distributions

Inasmuch as the tension shell shapes were calculated by assuming a Newtonian pressure distribution, a knowledge of the actual pressure distribution was considered desirable in order to evaluate the validity of this assumption. Pressure models of the shapes with length—base-radius ratios of 0.6 and 0.8 were tested at several Reynolds numbers, and the results are presented as figure 15. A pressure orifice was located in

the nose of each model to obtain the total pressure behind a normal shock. The experimental pressure distributions indicated that Newtonian theory is not adequate for predicting pressure distributions for tension shell shapes. The schlieren photographs of these two models (fig. 10) indicate that the disagreement between experimental and theoretical Newtonian pressure distributions should be expected inasmuch as the shock patterns do not follow the body contours as would be required for Newtonian flow. Also, the theoretical Newtonian pressure distributions do not include the centrifugal-force contribution of the flow adjacent to the concave surfaces of the models. For the longer shapes which have extensive flow separation, greater differences between experiment and theory would be expected.

#### Heat-Transfer Data at Angles of Attack

Data collected from tests of the heating-distribution models at various angles of attack are presented in figure 16 as nondimensionalized isotherm patterns. Tests were made for the models with values of  $l/r_b$  of 0.6 and 0.8 and with a value of  $R_n/r_b$  of approximately zero at a Reynolds number of  $0.09 \times 10^6$ . For the case of radiation-equilibrium conditions, isotherms can be related directly to local heating rates by the method given in the section entitled "Data Reduction"; hence, isotherm patterns represent heating-rate patterns. Figure 16 shows that the two models tested experienced a sharp increase in heating on the windward side as angle of attack increased. At the same time heating on the leeward side decreased. A comparison of radiation-equilibrium heating distributions for the two models at zero angle of attack is presented in figure 17. The heating on the model with  $l/r_b = 0.8$  decreased with the distance from the nose of the model up to a point and then began to increase. In contrast, the heating-rate distribution of the model with  $l/r_b = 0.6$  decreased continuously as the distance from the nose increased. Inasmuch as this rear section comprises the largest percentage of the total area of the surface, the total heating on the longer model was greater. An examination of the total-convective-heating-rate coefficients for the family of shapes (fig. 11) indicates that the total heating rates also increased with length for a range of  $l/r_b$  between 0.6 and 1.0. For values of  $l/r_b$  larger than 1.0, the total heating rates decreased with length. Figure 10 shows that flow separation was slight for models with length—base-radius ratios less than 1.0, but became quite extensive as  $l/r_b$  increased above 1.0. Therefore, it was concluded that for the tension shell shapes an increase in model length incurs a rise in total heating rate only as long as extensive flow separation is avoided.

#### Flow-Field Comparisons

Comparative schlieren photographs of the aerodynamic-force, pressure-distribution, and heating-distribution models ( $l/r_b = 0.6$  and  $0.8$ ;  $R_n/r_b = 0$ ) for tests at zero angle of

attack are presented in figure 18. The comparison is necessitated by the fact that model wall temperatures for the three types of tests varied widely, and, according to reference 5, wall temperatures might have an effect on the extent of flow separation. The pressure models have a slightly blunted nose due to the stagnation orifice which affects the shock pattern in this area. However, examination of figure 18 indicates that at each value of  $l/r_b$  there were no significant differences in the flow fields for the three different models at zero angle of attack. Comparison of schlieren photographs for models at angles of attack other than zero also indicated no basic differences in the flow fields.

## CONCLUSIONS

An exploratory experimental study of tension shell shapes for use in unmanned planetary entry has been conducted. The tests were performed in the 7-inch (17.8-cm) Mach 7 pilot tunnel at the Langley Research Center at a stream stagnation temperature of approximately 3420° R (1900° K) and at Reynolds numbers ranging from  $0.043 \times 10^6$  to  $0.173 \times 10^6$ . The test medium was the combustion products of methane and air. The data collected were aerodynamic force and moment measurements, pressure distributions, and heating rates. The following conclusions were reached:

1. Some tension shell configurations deserve consideration for use as unmanned planetary-entry vehicles, as indicated by maximum measured drag coefficients of about 1.65.
2. Flow separation from the surface of a tension shell shape was the most important factor affecting its aerodynamic characteristics. The major significance of model length and nose bluntness was the effect on the extent of flow separation.
3. Measured pitching-moment coefficients for the models with length—base-radius ratios of 0.6 and 0.8 and nose-radius—base-radius ratios of 0 were slightly positive for nearly all angles of attack at which tests were made.
4. The experimental pressure distributions obtained for the models with length—base-radius ratios of 0.6 and 0.8 indicated that the assumption of a theoretical Newtonian pressure distribution is not valid.
5. Increasing the length of the tension shell configurations incurred attendant increases in the total convective heating if the flow remained attached to the body surface.

Langley Research Center,  
National Aeronautics and Space Administration,  
Langley Station, Hampton, Va., June 4, 1965.

## APPENDIX

### CONVERSION OF U. S. CUSTOMARY UNITS TO SI UNITS

The International System of Units (SI) was adopted by the Eleventh General Conference on Weights and Measures, Paris, October 1960, in Resolution No. 12 (ref. 4). Conversion factors for the units used herein are given in the following table:

Physical quantity	U. S. Customary Unit	Conversion factor (*)	SI unit
Length	in.	0.0254	meters (m)
Local heating parameter	Btu/sec-ft <sup>2</sup> -°R	20428	watts/meter <sup>2</sup> -degrees Kelvin $\left(\frac{W}{m^2-°K}\right)$
Pressure	psi = lbf/in <sup>2</sup>	6895	newtons/meter <sup>2</sup> (N/m <sup>2</sup> )
Temperature	°R	5/9	degrees Kelvin (°K)
Thermal efficiency	Btu/lbm	2324	joules/kilogram (J/kg)

\*Multiply value given in U. S. Customary Units by conversion factor to obtain equivalent value in SI units.

Prefixes to indicate multiple of units are as follows:

Prefix	Multiple
mega (M)	10 <sup>6</sup>
kilo (k)	10 <sup>3</sup>
centi (c)	10 <sup>-2</sup>

## REFERENCES

1. Anderson, Roger A. : Structures Technology – 1964. Astronaut. Aeron. , vol. 2, no. 12, Dec. 1964, pp. 14-20.
2. Roberts, Leonard: Entry Into Planetary Atmospheres. Astronaut. Aeron. , vol. 2, no. 10, Oct. 1964, pp. 22-29.
3. Anderson, Melvin S. ; Robinson, James C. ; Bush, Harold G. ; and Fralich, Robert W. : A Tension Shell Structure for Application to Entry Vehicles. NASA TN D-2675, 1965.
4. Mechtly, E. A. : The International System of Units – Physical Constants and Conversion Factors. NASA SP-7012, 1964.
5. Centolanzi, Frank J. : Heat Transfer to Blunt Conical Bodies Having Cavities to Promote Separation. NASA TN D-1975, 1963.
6. Weinstein, Irving; and Howell, Robert R. : Technique for Measuring High-Temperature Isotherm Patterns on Aerodynamically Heated Models With Experimental Results. NASA TN D-2769, 1965.
7. Leyhe, Edward W. ; and Howell, Robert R. : Calculation Procedure for Thermodynamic, Transport, and Flow Properties of the Combustion Products of a Hydrocarbon Fuel Mixture Burned in Air With Results for Ethylene-Air and Methane-Air Mixtures. NASA TN D-914, 1962.
8. Siviter, James H. , Jr. ; and Strass, H. Kurt: An Investigation of a Photographic Technique of Measuring High Surface Temperatures. NASA TN D-617, 1960.
9. Bernot, Peter T. : Longitudinal Stability Characteristics of Several Proposed Planetary Entry Vehicles at Mach 6.73. NASA TN D-2785, 1965.

TABLE I.- COORDINATES OF MODELS A AND B

$$[A^2 = 1.523]$$

r/r <sub>b</sub>	x/r <sub>b</sub> for:	
	Model A (R <sub>n</sub> /r <sub>b</sub> = 0.1333)	Model B (R <sub>n</sub> /r <sub>b</sub> = 0.0125)
0	1.1160	1.9220
.10	1.0708	.9196
.20	.8833	.8541
.30	.6872	.6872
.40	.5104	.5104
.50	.3566	.3566
.60	.2298	.2298
.70	.1301	.1301
.80	.0584	.0584
.90	.0148	.0148
1.00	.0000	.0000

TABLE II.- COORDINATES OF FAMILY OF TENSION SHELL SHAPES

$$[R_n/r_b = 0]$$

r/r <sub>b</sub>	x/r <sub>b</sub> for:						
	l/r <sub>b</sub> = 0.6 (A <sup>2</sup> = 0.835)	l/r <sub>b</sub> = 0.8 (A <sup>2</sup> = 1.058)	l/r <sub>b</sub> = 1.0 (A <sup>2</sup> = 1.257)	l/r <sub>b</sub> = 1.192 (A <sup>2</sup> = 1.423)	l/r <sub>b</sub> = 1.5 (A <sup>2</sup> = 1.663)	l/r <sub>b</sub> = 2.0 (A <sup>2</sup> = 1.973)	l/r <sub>b</sub> = 3.0 (A <sup>2</sup> = 2.427)
0	0.6000	0.8000	1.0000	1.1920	1.5000	2.0000	3.000
.05	.5535	.7368	.9193	1.0944	1.3730	1.8240	2.720
.10	.5073	.6738	.8392	.9976	1.2474	1.6496	2.443
.15	.4616	.6119	.7603	.9008	1.1237	1.4790	2.172
.20	.4168	.5512	.6830	.8080	1.0036	1.3136	1.912
.25	.3731	.4921	.6083	.7184	.8875	1.1546	1.664
.30	.3307	.4350	.5361	.6304	.7762	1.0038	1.431
.35	.2900	.3804	.4672	.5488	.6717	.8622	1.215
.40	.2512	.3284	.4022	.4688	.5133	.7305	1.017
.45	.2164	.2794	.3410	.3968	.4807	.6096	.837
.50	.1799	.2337	.2842	.3296	.3984	.4999	.673
.55	.1480	.1916	.2322	.2688	.3226	.4004	.537
.60	.1187	.1531	.1849	.2144	.2547	.3144	.415
.65	.0923	.1186	.1427	.1648	.1949	.2388	.310
.70	.0687	.0882	.1058	.1216	.1432	.1741	.223
.75	.0485	.0621	.0742	.0848	.0995	.1201	.153
.80	.0316	.0403	.0480	.0544	.0640	.0763	.096
.85	.0182	.0231	.0274	.0304	.0358	.0428	.053
.90	.0084	.0106	.0125	.0144	.0160	.0190	.023
.95	.0022	.0027	.0032	.0036	.0040	.0047	.005
1.00	.0000	.0000	.0000	.0000	.0000	.0000	.000

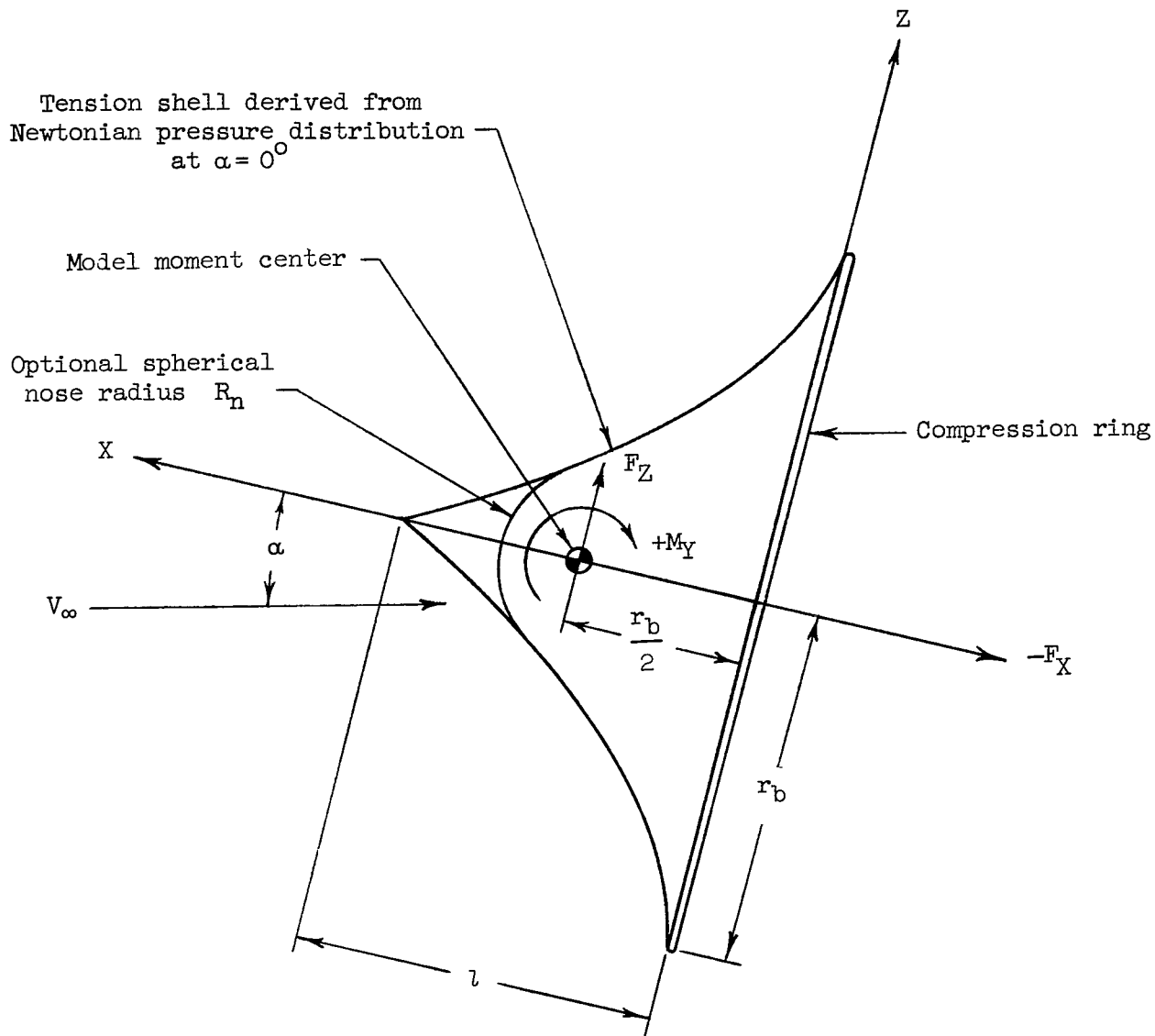
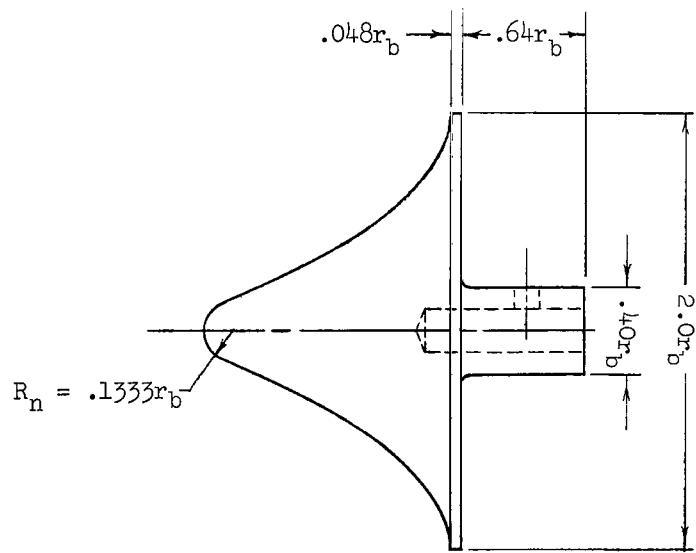
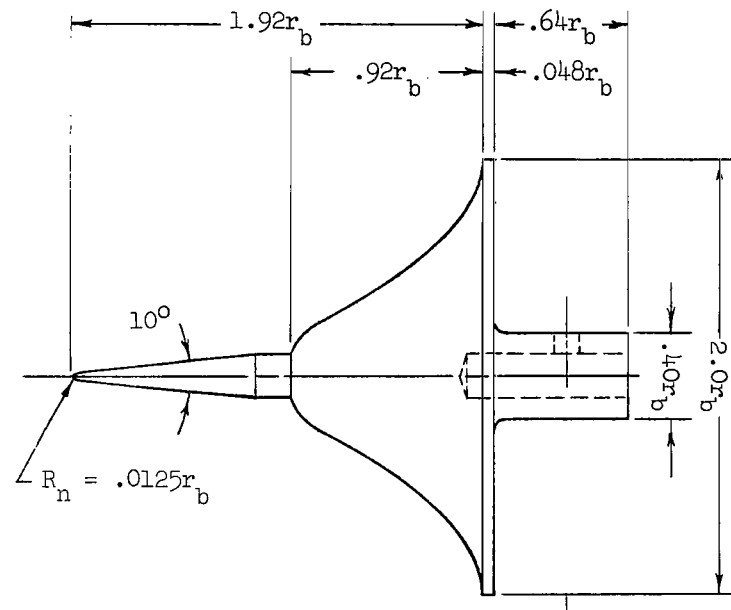


Figure 1.- Sketch indicating the orientation of model axes and force reference axes.

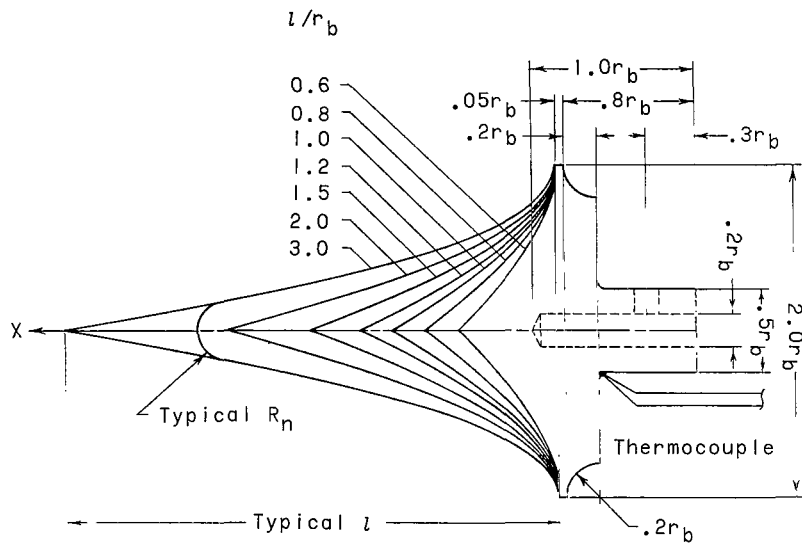


(a) Model A.

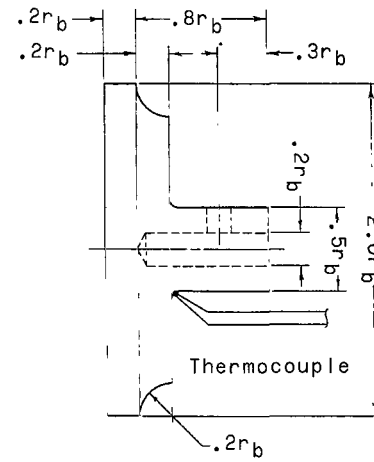


(b) Model B.

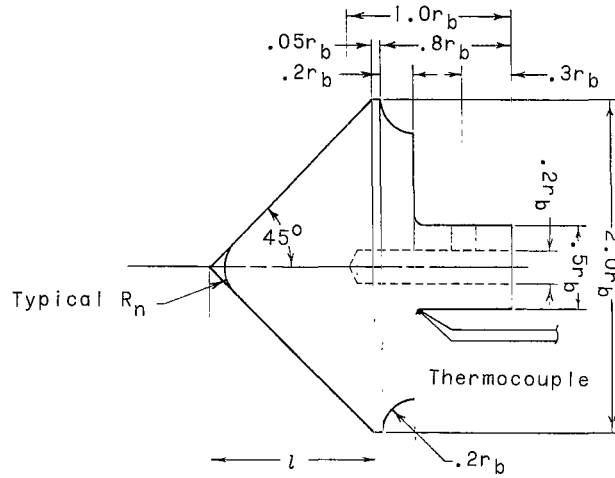
Figure 2.- Pertinent dimensions of models A and B. Maximum model radius,  $r_b = 0.625$  in. (1.59 cm).



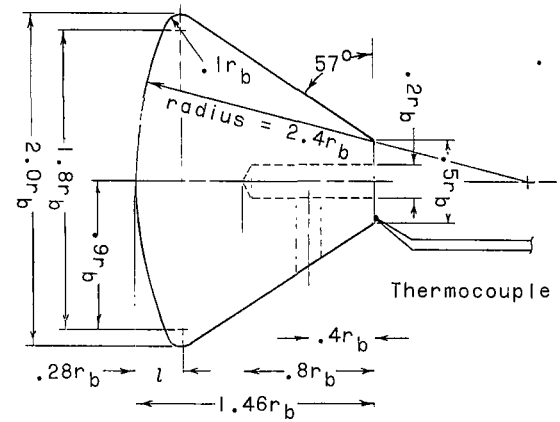
(a) Tension shell shapes.



(b) Flat disk.

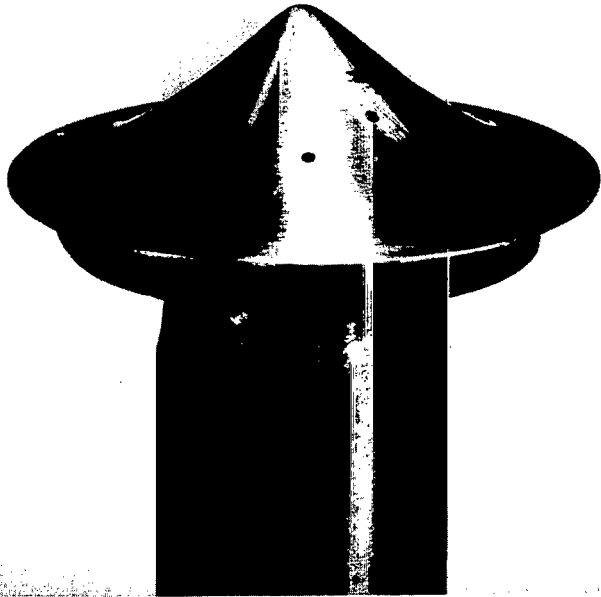
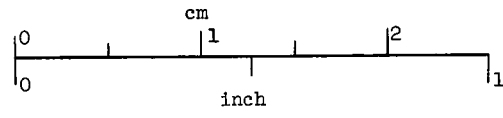


(c)  $45^\circ$  half-angle cone.



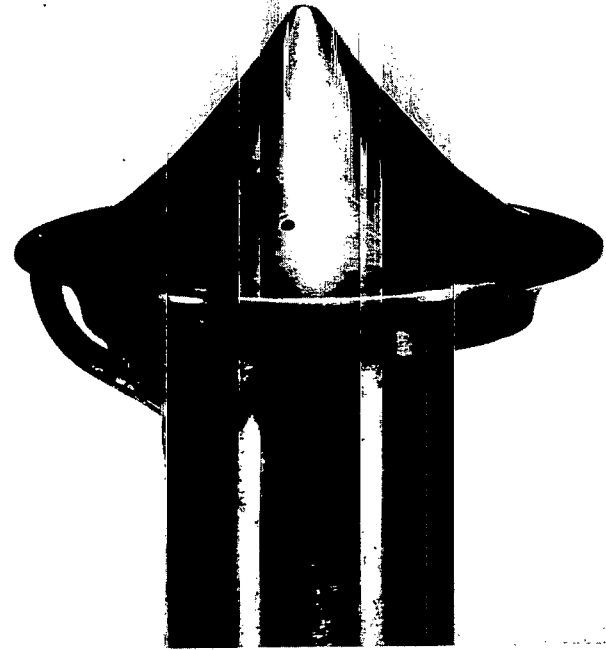
(d) Blunt entry body.

Figure 3.- Pertinent dimensions of tension shell models and reference models. Maximum model radius  $r_b = 0.625$  in. (1.59 cm).



$$\frac{l}{r_b} = 0.6$$

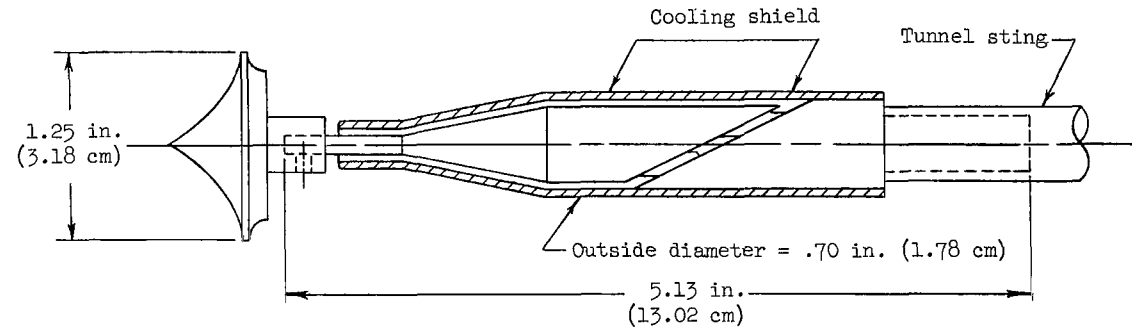
L-64-7339



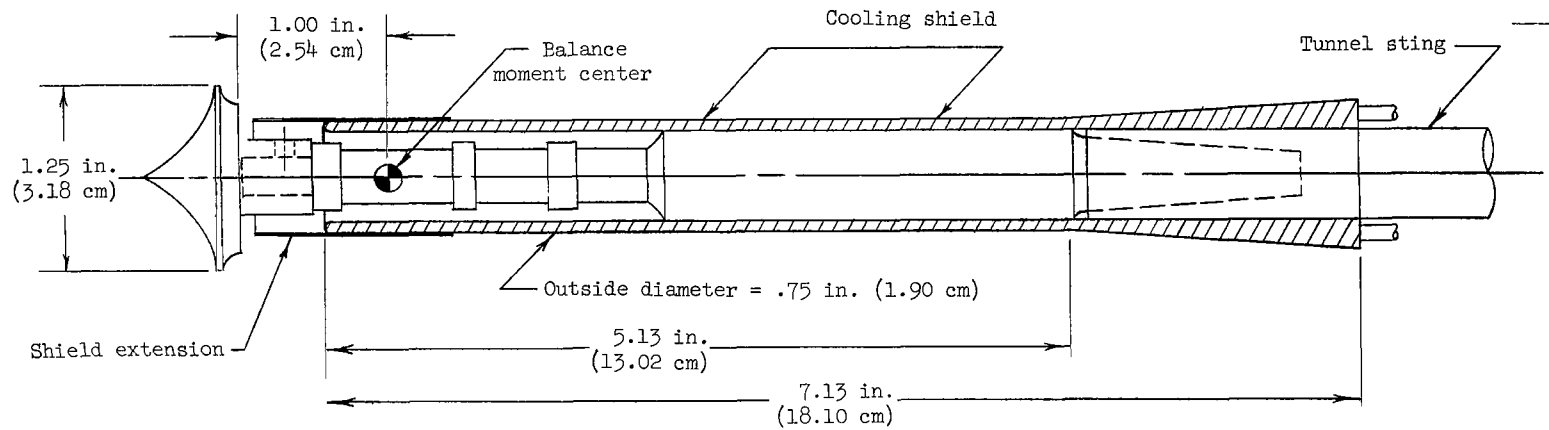
$$\frac{l}{r_b} = 0.8$$

L-64-7338

Figure 4.- Photographs of pressure models.



(a) Single-component balance (axial force).



(b) Six-component balance.

Figure 5.- General arrangements of strain-gage balances used in force tests.

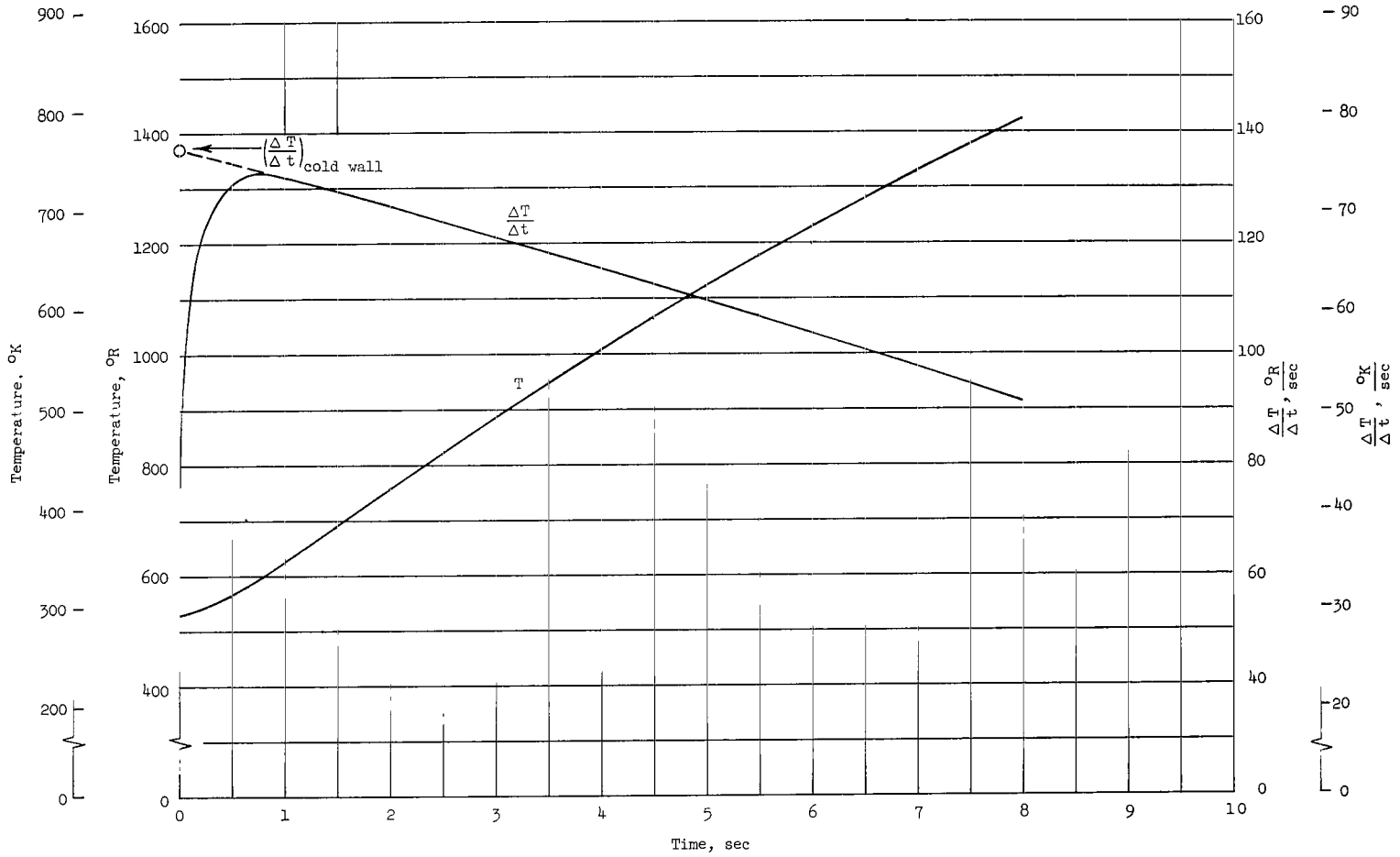


Figure 6.- Variation of model temperature and temperature gradient with time for typical test of copper force model.

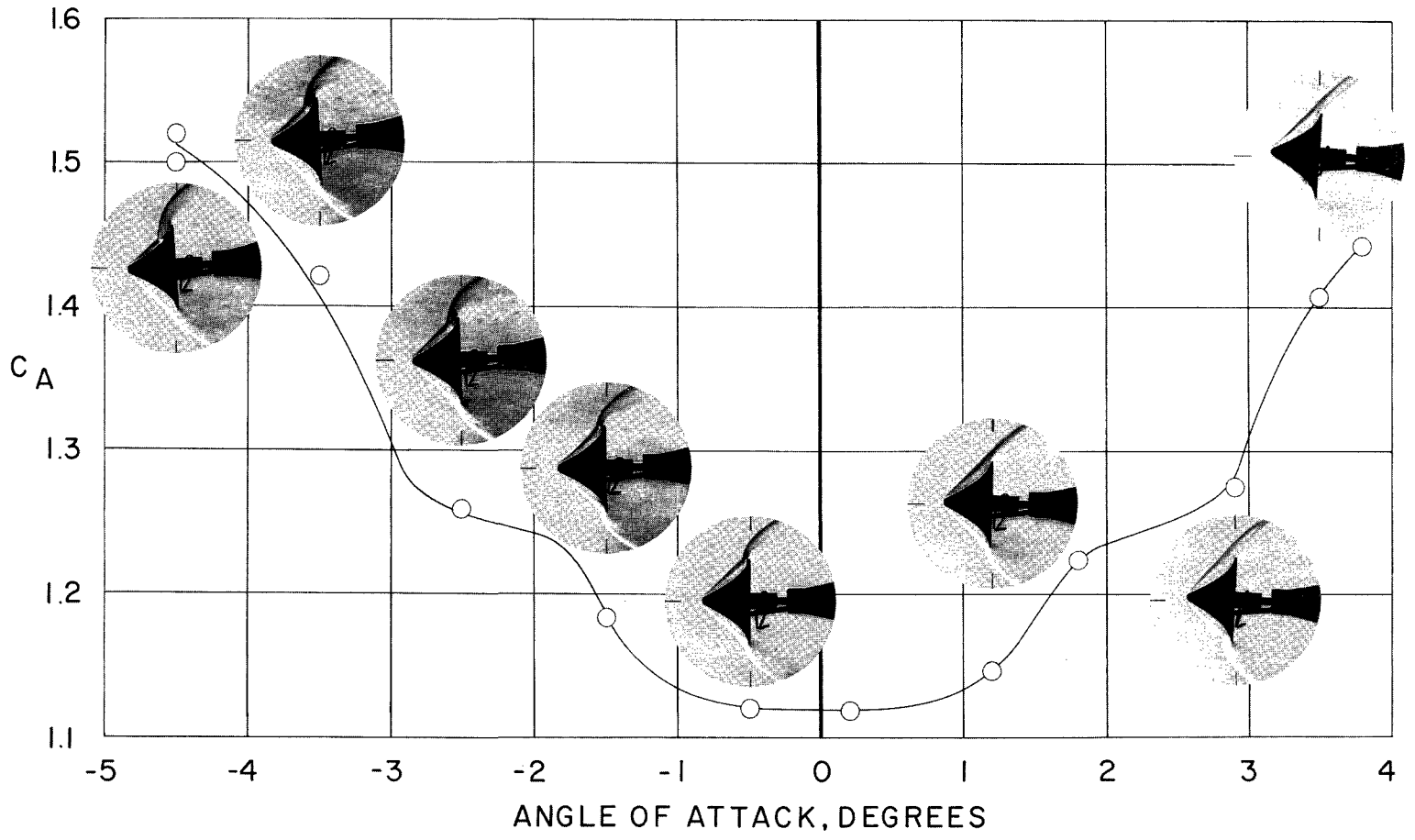


Figure 7.- Variation of axial-force coefficient with angle of attack for model A.

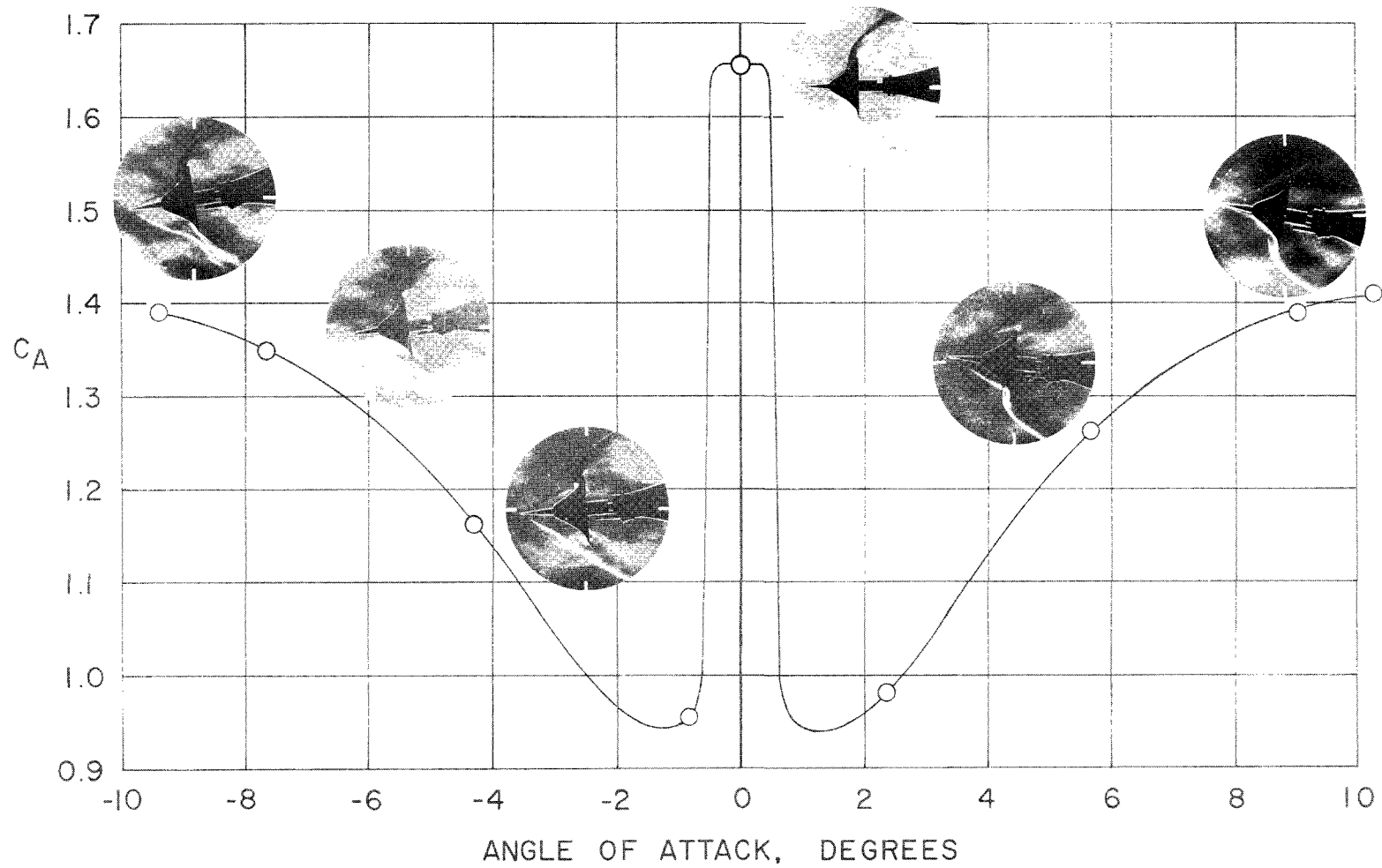


Figure 8.- Variation of axial-force coefficient with angle of attack for model B.

L-65-147

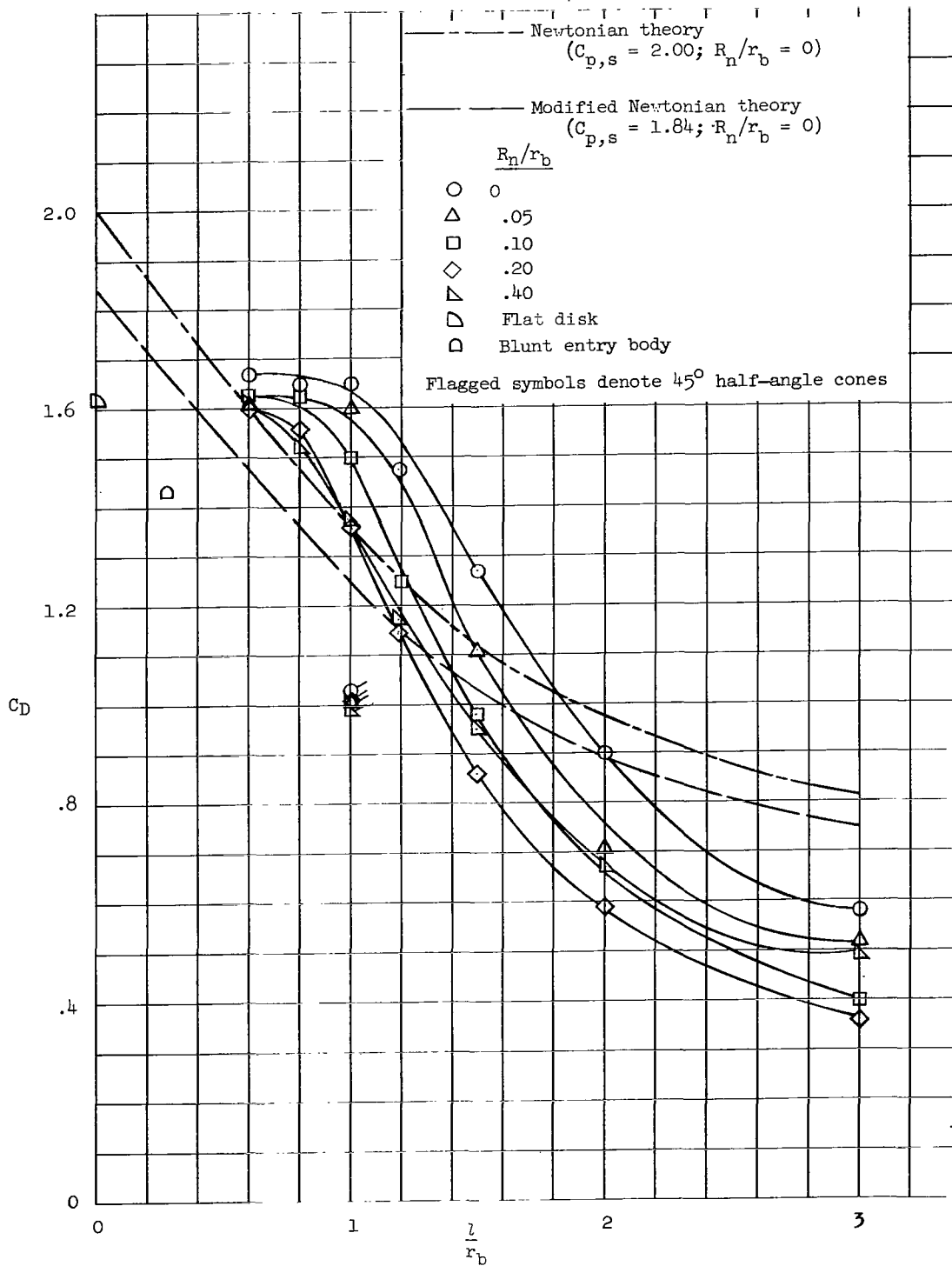


Figure 9.- Variation of drag coefficient with length for the family of tension shell shapes showing the effect of nose bluntness.  
 $\alpha = 0^\circ$ ;  $R_D = 0.08 \times 10^6$ .

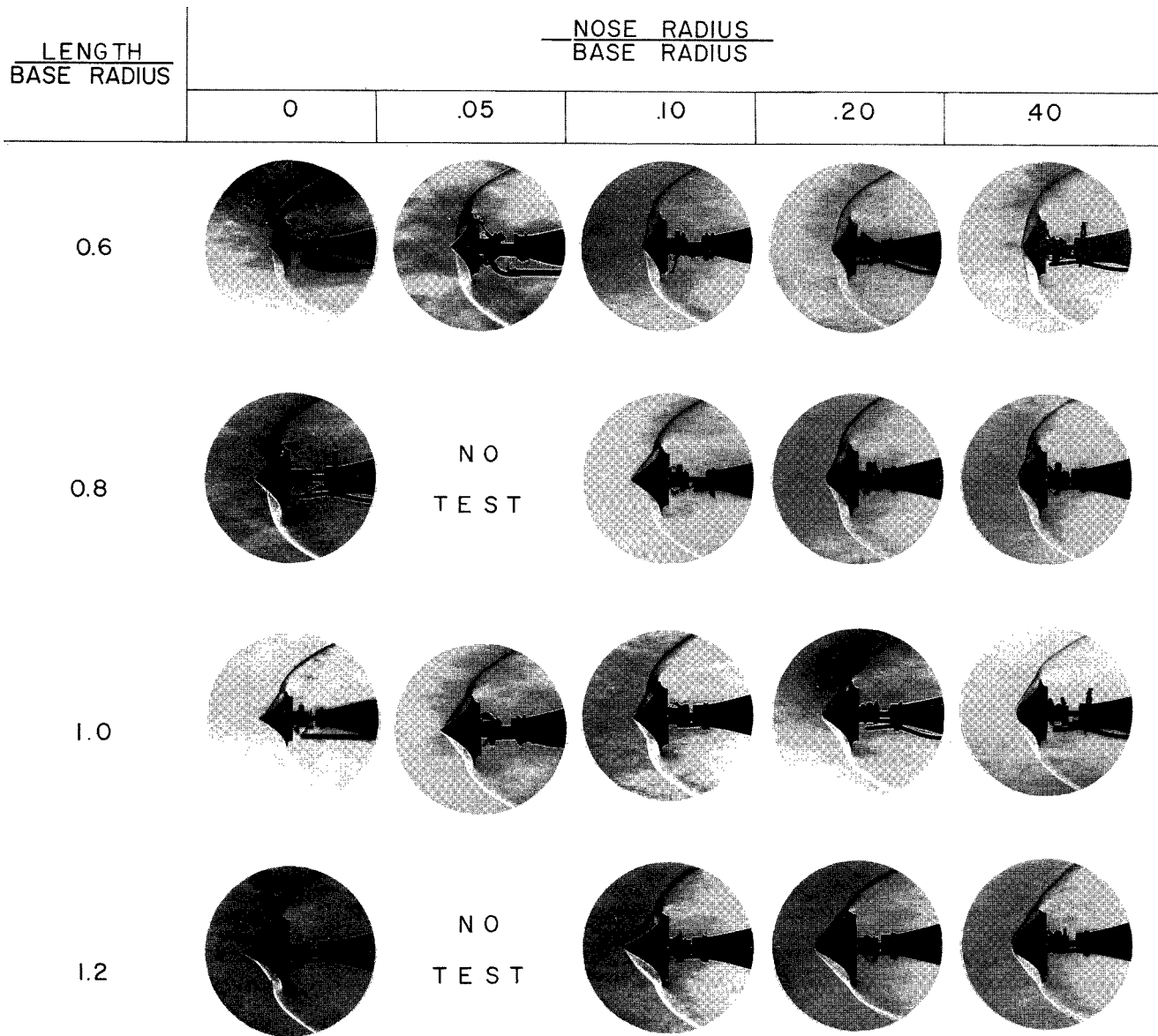


Figure 10.- Schlieren photographs for tests of family of tension shell shapes and 45° half-angle cone.  $\alpha = 0^\circ$ ;  $R_D = 0.08 \times 10^6$ . L-65-148

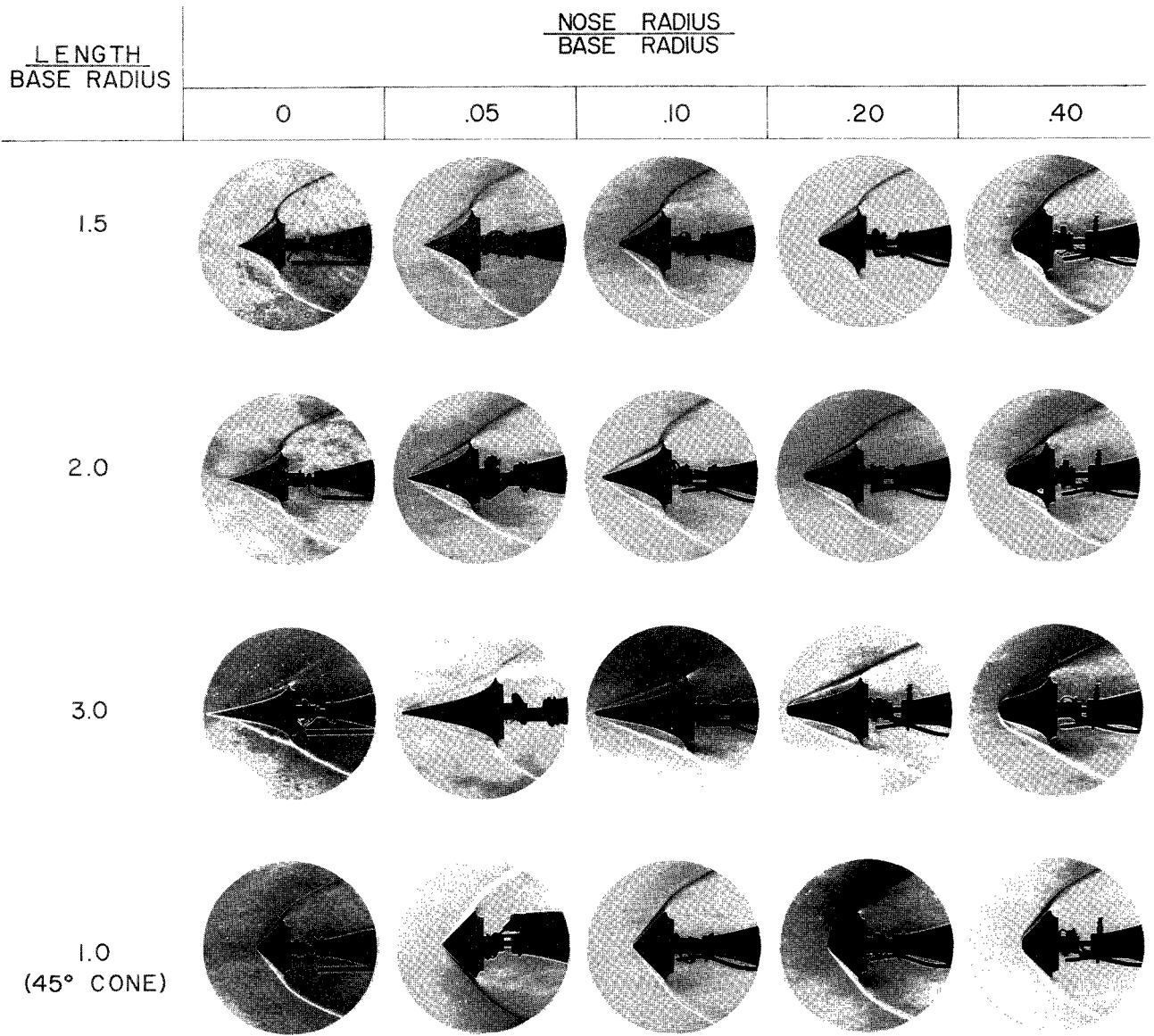


Figure 10.- Concluded.

L-65-149

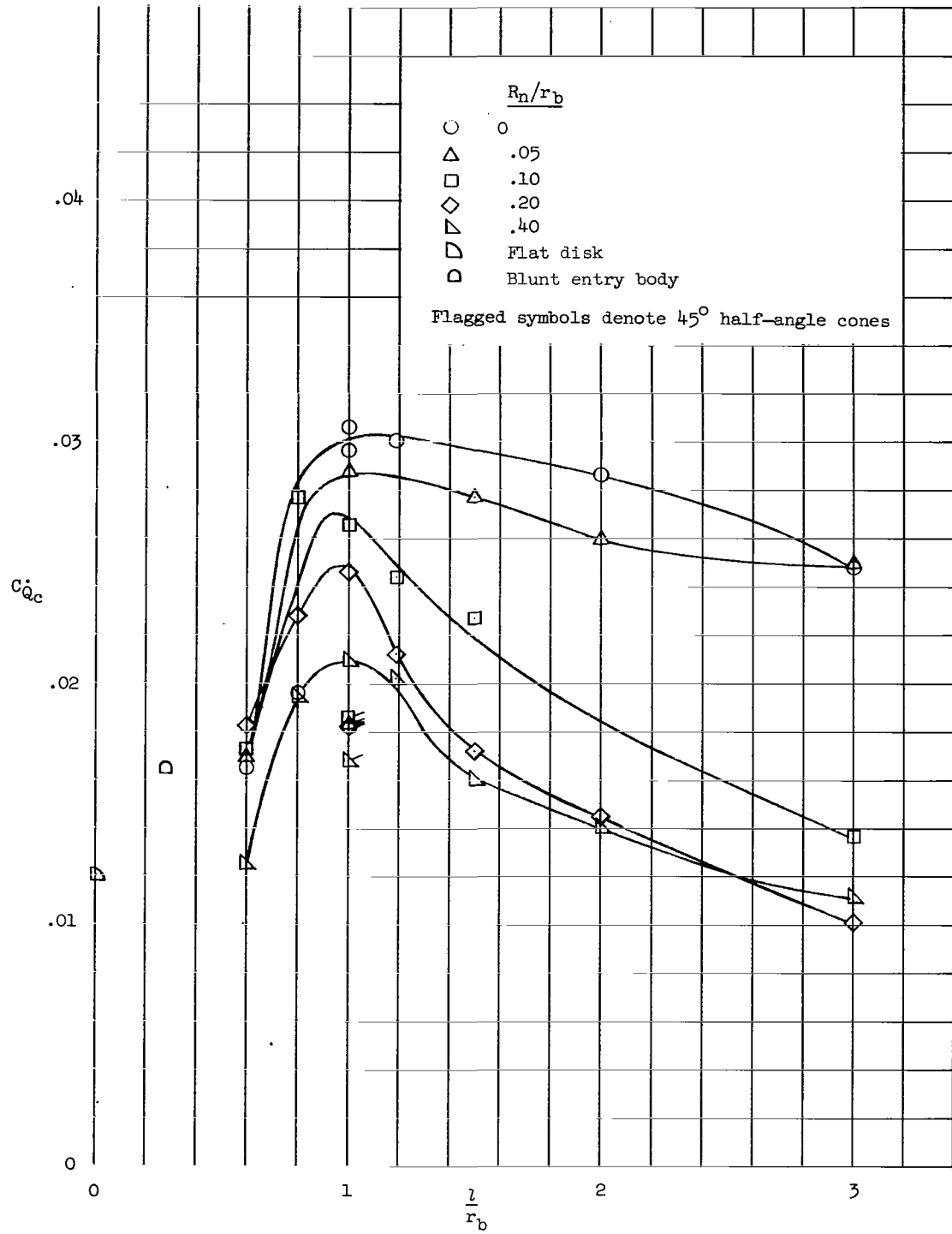


Figure 11.- Variation of convective-heating-rate coefficient with length for the family of tension shell shapes showing the effect of nose bluntness.  $\alpha = 0^\circ$ ;  $R_D = 0.08 \times 10^6$ .

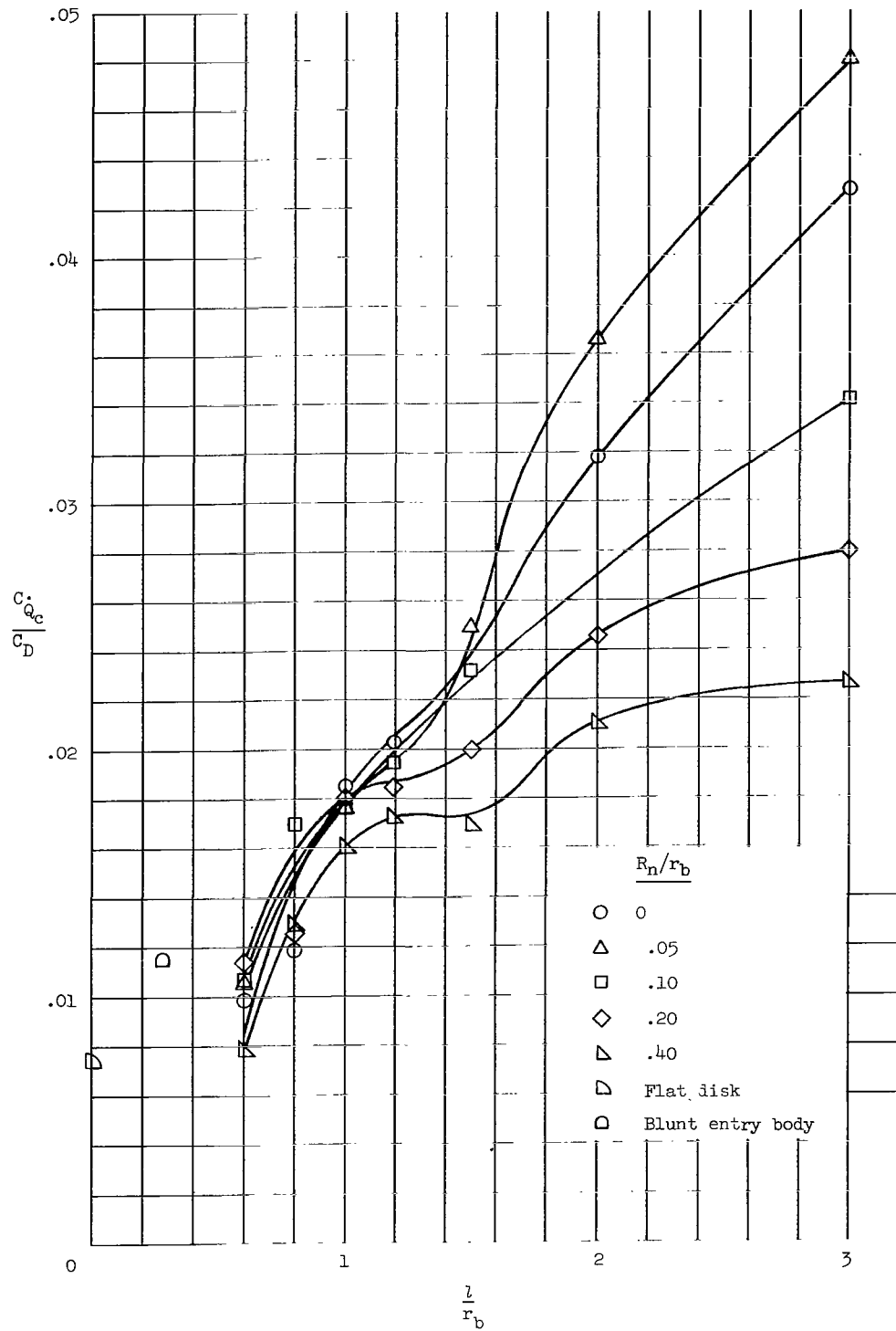
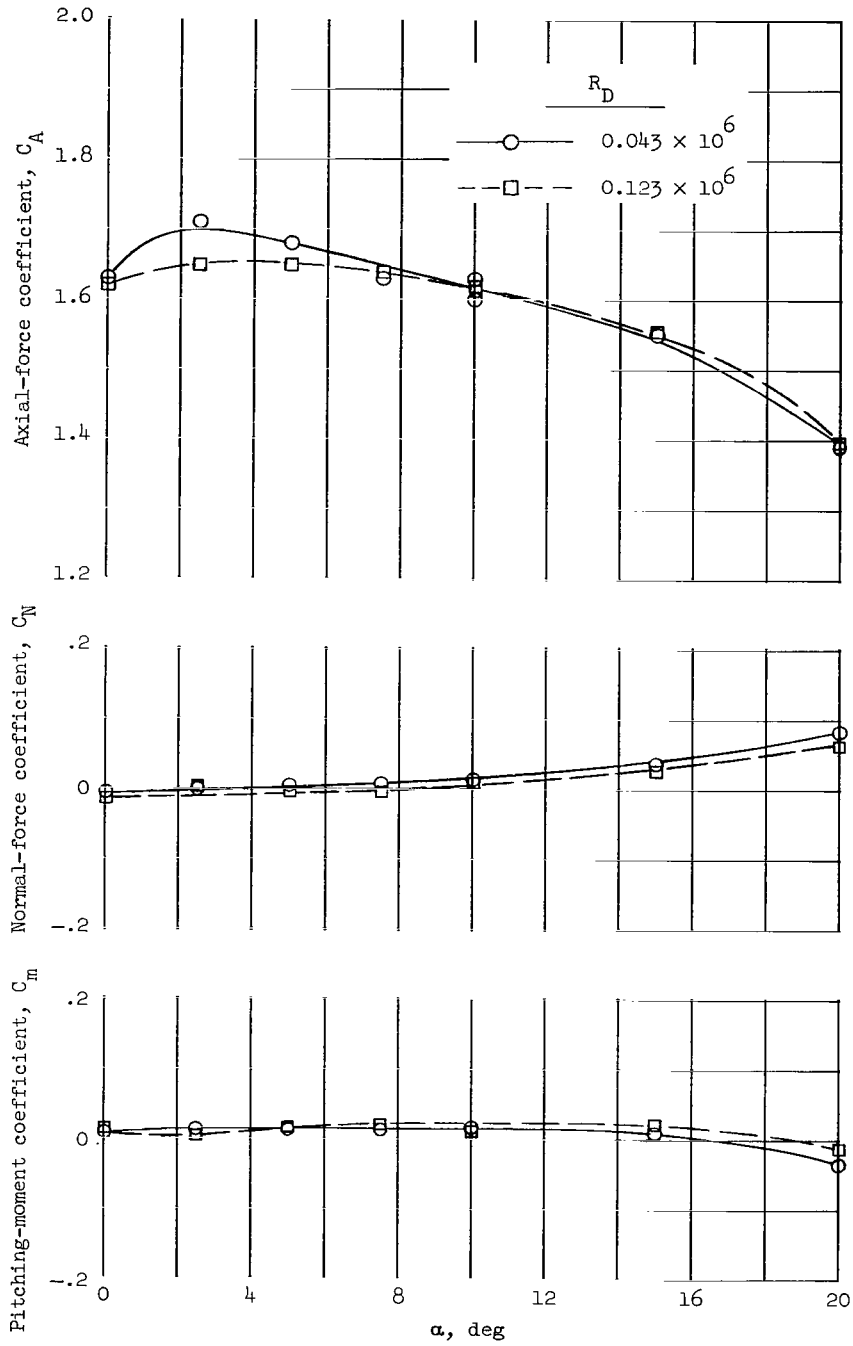
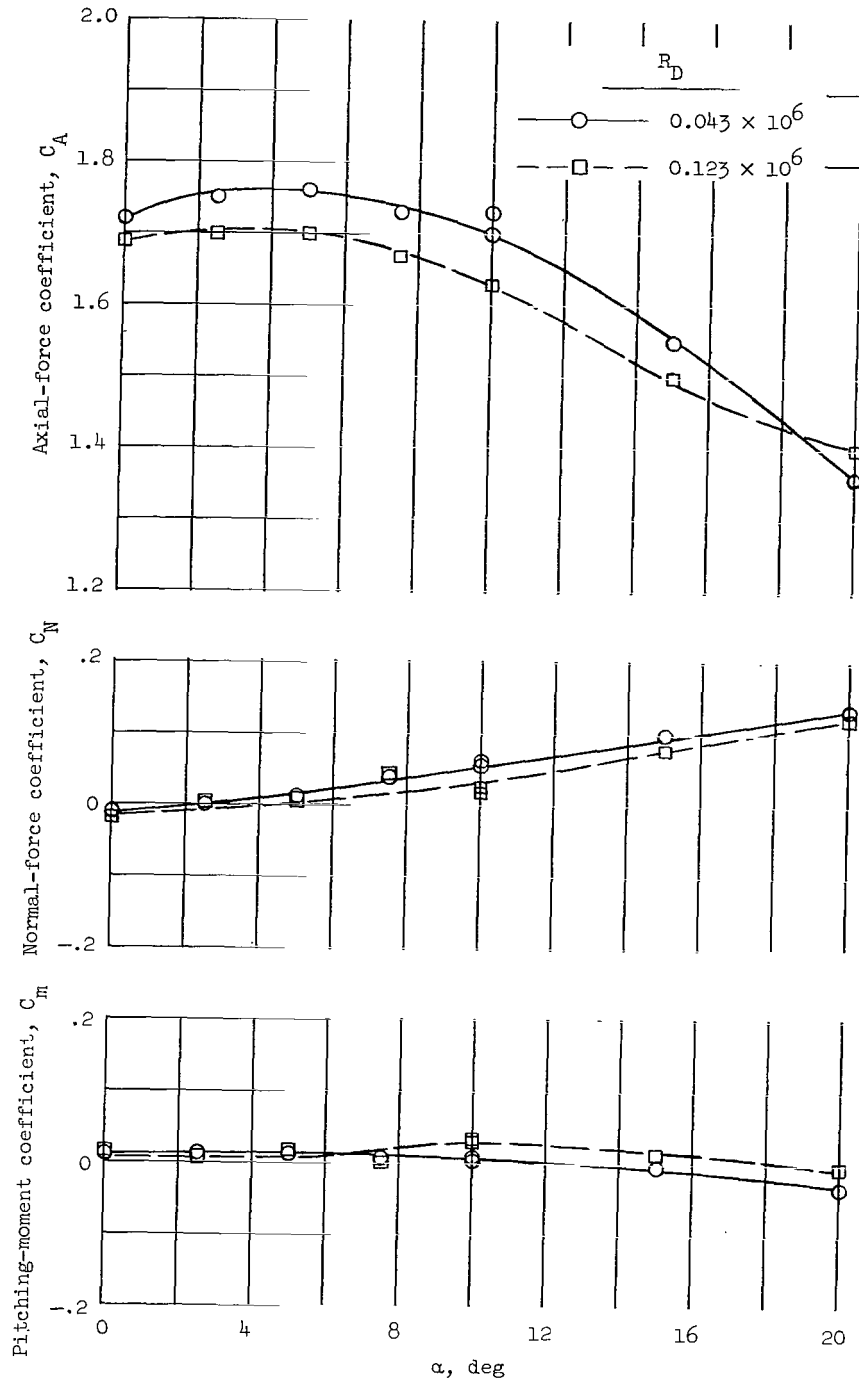


Figure 12.- Variation of the ratio of convective-heating-rate coefficient to drag coefficient with length for the family of tension shell shapes showing the effect of nose bluntness.  $\alpha = 0^\circ$ ;  $R_D = 0.08 \times 10^6$ .



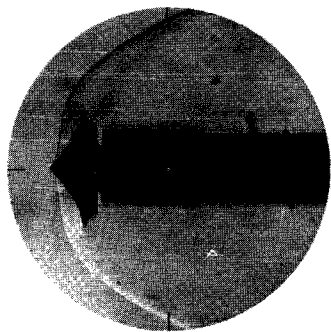
(a)  $l/r_b = 0.6$ .

Figure 13.- Variation of axial-force, normal-force, and pitching-moment coefficients with angle of attack for shapes with  $l/r_b$  values of 0.6 and 0.8 and  $R_D/r_b = 0$ .



(b)  $l/r_D = 0.8$ .

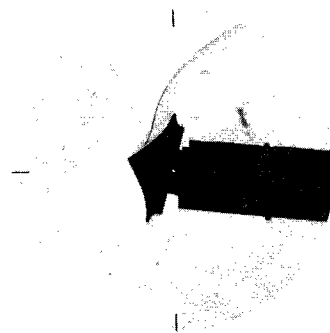
Figure 13.- Concluded.



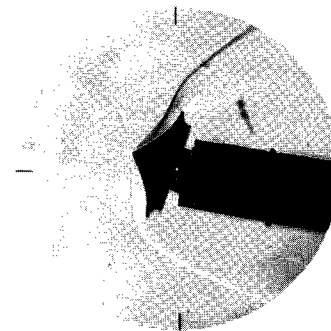
$\alpha = 0^\circ$



$\alpha = 10^\circ$

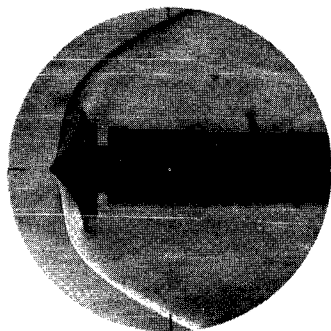


$\alpha = 15^\circ$

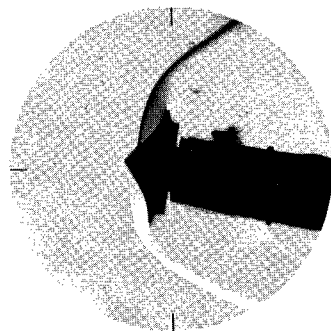


$\alpha = 20^\circ$

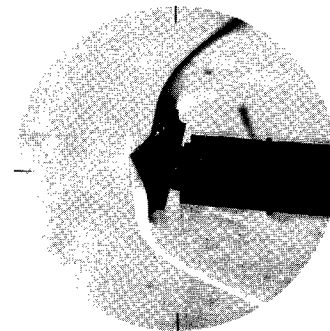
$R_D = 0.043 \times 10^6$



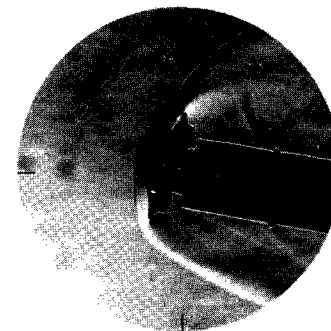
$\alpha = 0^\circ$



$\alpha = 10^\circ$



$\alpha = 15^\circ$



$\alpha = 20^\circ$

$R_D = 0.123 \times 10^6$

(a)  $l/r_b = 0.6$ .

L-65-150

Figure 14.- Schlieren photographs of bodies with  $l/r_b$  values of 0.6 and 0.8 at various angles of attack.

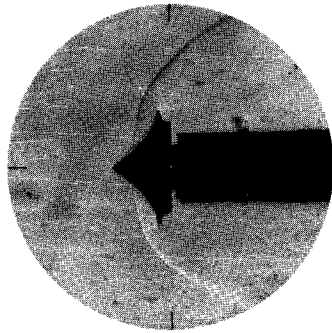
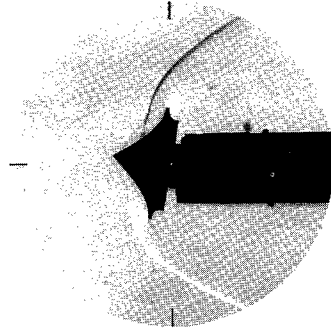
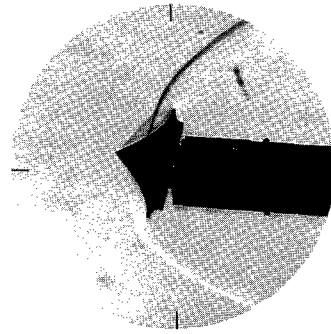
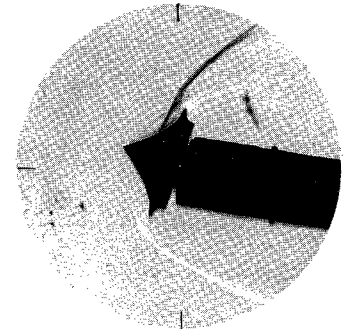
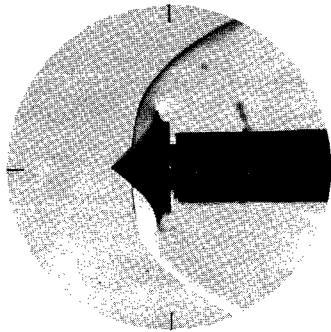
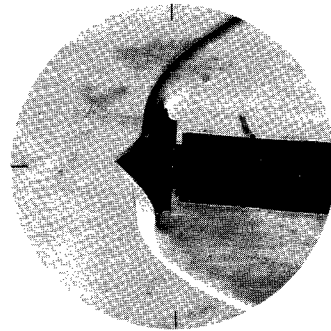
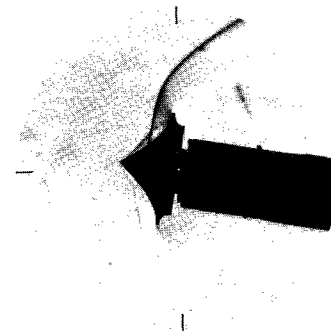
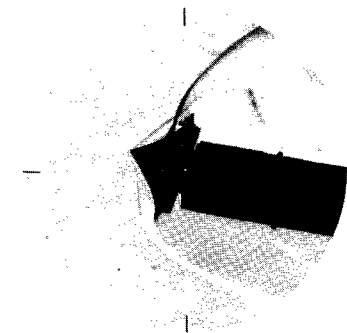
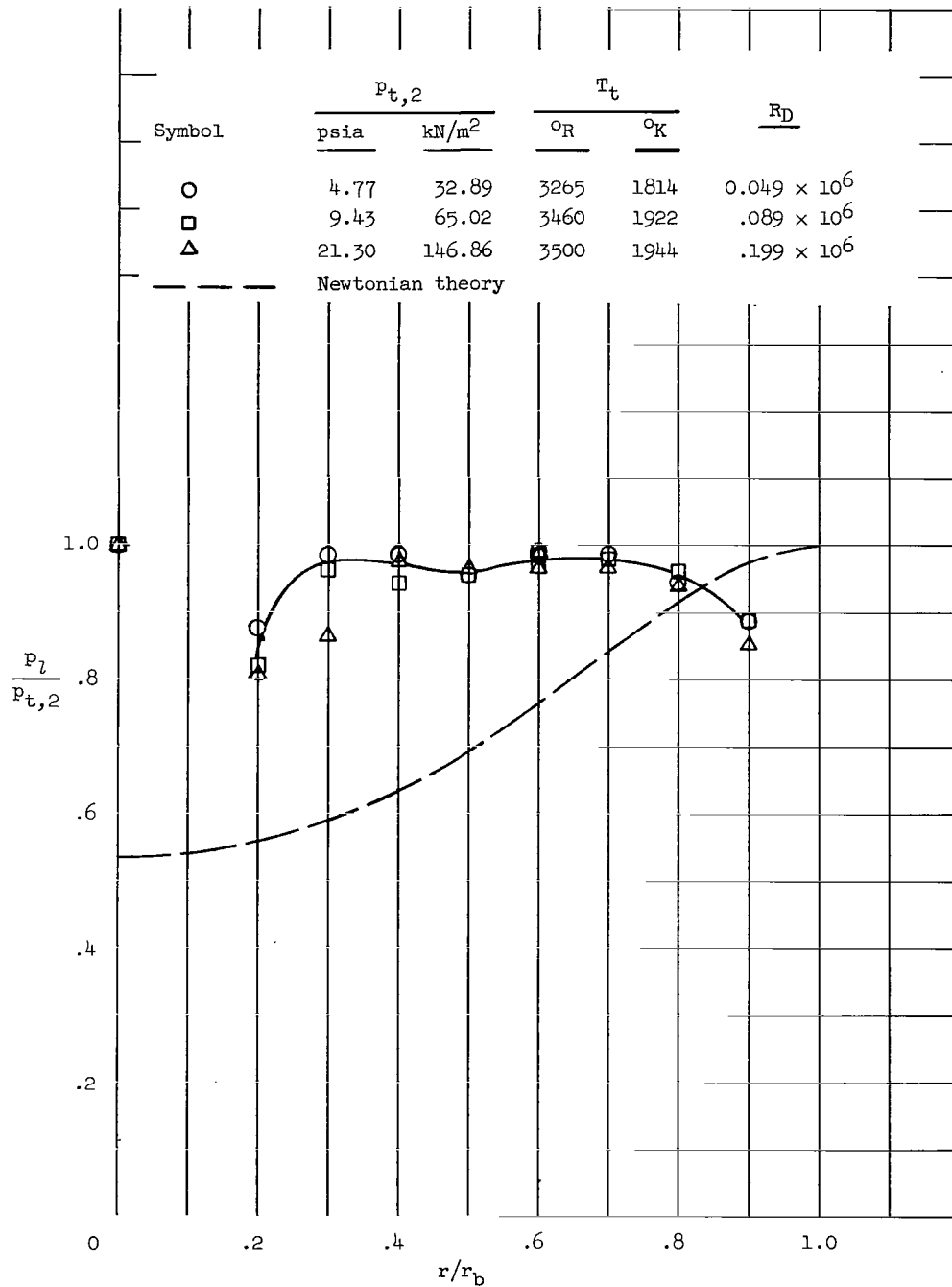
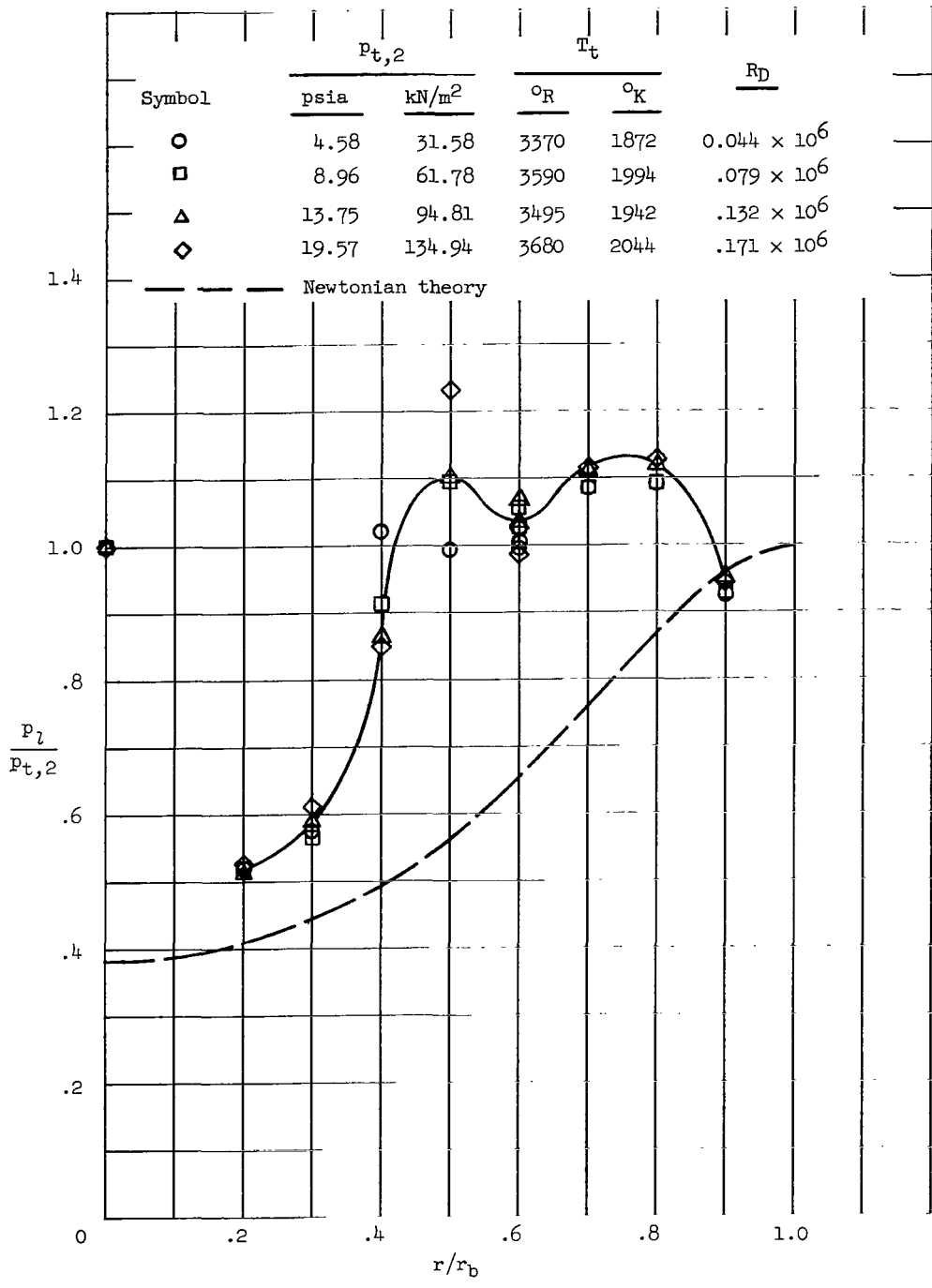
 $\alpha = 0^\circ$  $\alpha = 10^\circ$  $\alpha = 15^\circ$  $\alpha = 20^\circ$  $R_D = 0.043 \times 10^6$  $\alpha = 0^\circ$  $\alpha = 5^\circ$  $\alpha = 10^\circ$  $\alpha = 20^\circ$  $R_D = 0.123 \times 10^6$ (b)  $\psi r_b = 0.8$ .

Figure 14.- Concluded.



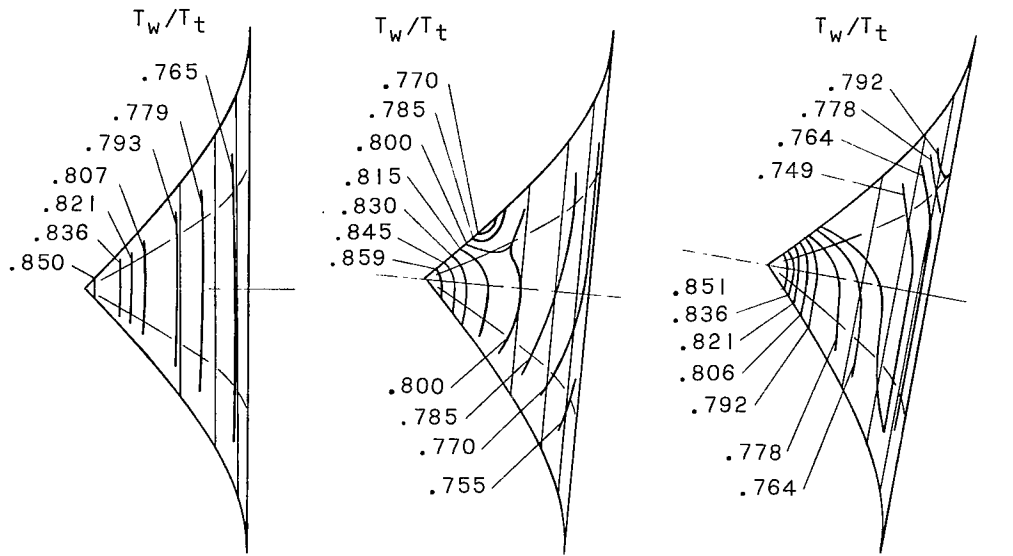
(a)  $l/r_b = 0.6$ .

Figure 15.- Nondimensionalized surface pressures plotted against radial distances from model axis in terms of base radius for models with  $l/r_b$  values of 0.6 and 0.8 and  $R_n/r_b = 0$ .



(b)  $u/r_b = 0.8$ .

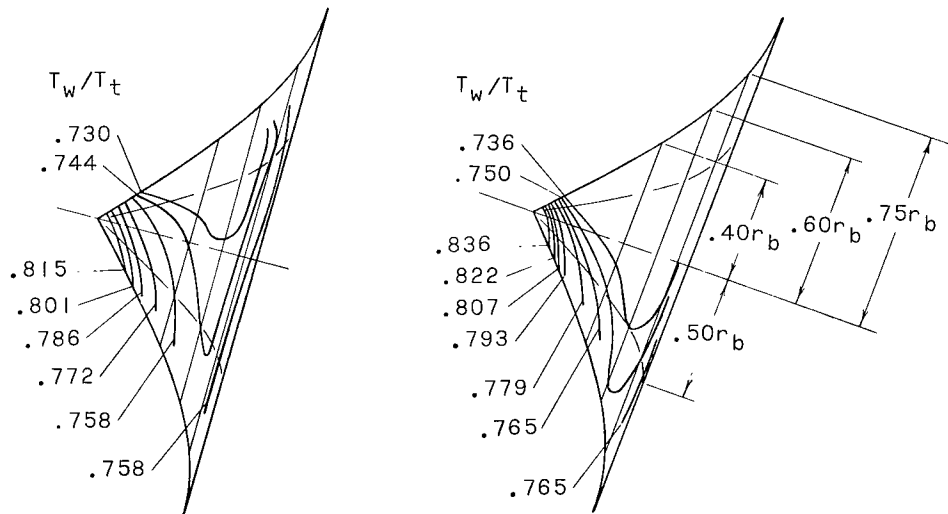
Figure 15.- Concluded.



$\alpha = 0^\circ$   
 $T_t = 3480^\circ \text{ R } (1933^\circ \text{ K})$

$\alpha = 5^\circ$   
 $T_t = 3385^\circ \text{ R } (1881^\circ \text{ K})$

$\alpha = 10^\circ$   
 $T_t = 3420^\circ \text{ R } (1900^\circ \text{ K})$

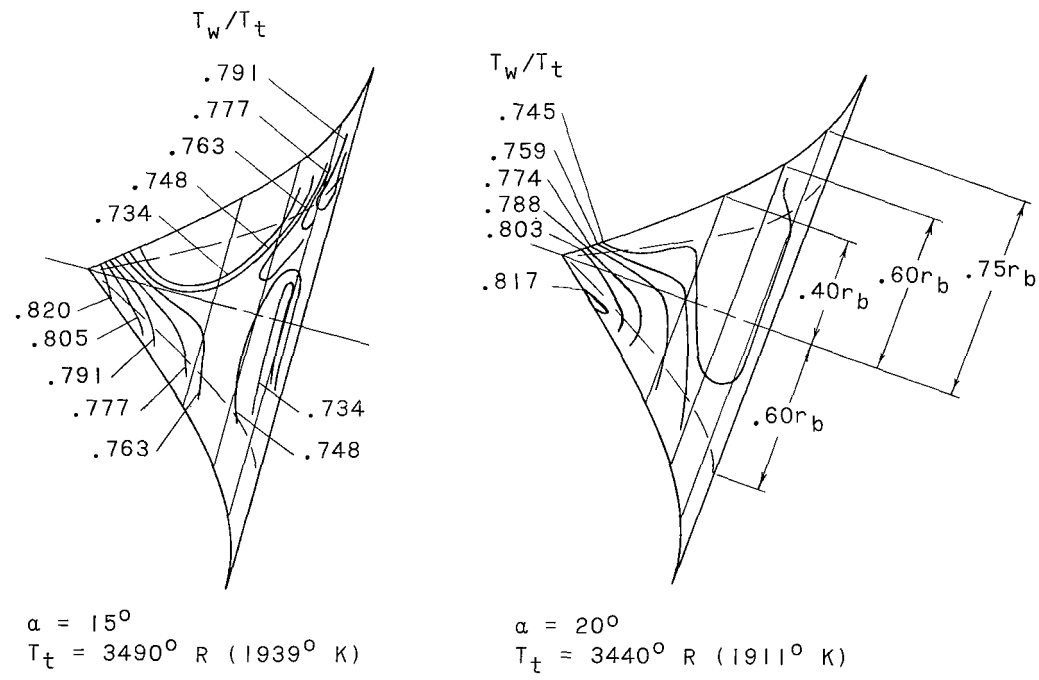
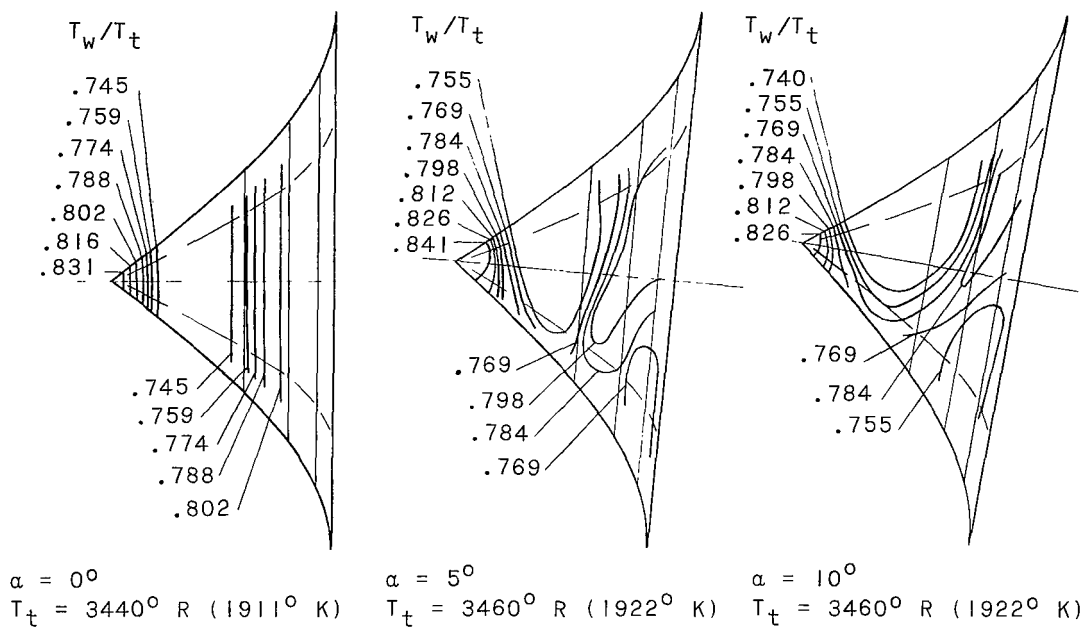


$\alpha = 15^\circ$   
 $T_t = 3510^\circ \text{ R } (1950^\circ \text{ K})$

$\alpha = 20^\circ$   
 $T_t = 3480^\circ \text{ R } (1933^\circ \text{ K})$

(a)  $l/r_b = 0.6$ .

Figure 16.- Nondimensionalized surface isotherms at radiation-equilibrium conditions for bodies with  $l/r_b$  values of 0.6 and 0.8 at various angles of attack.  $R_n/r_b = 0$ ;  $R_D = 0.09 \times 10^6$ .



(b)  $l/r_b = 0.8$ .

Figure 16.- Concluded.

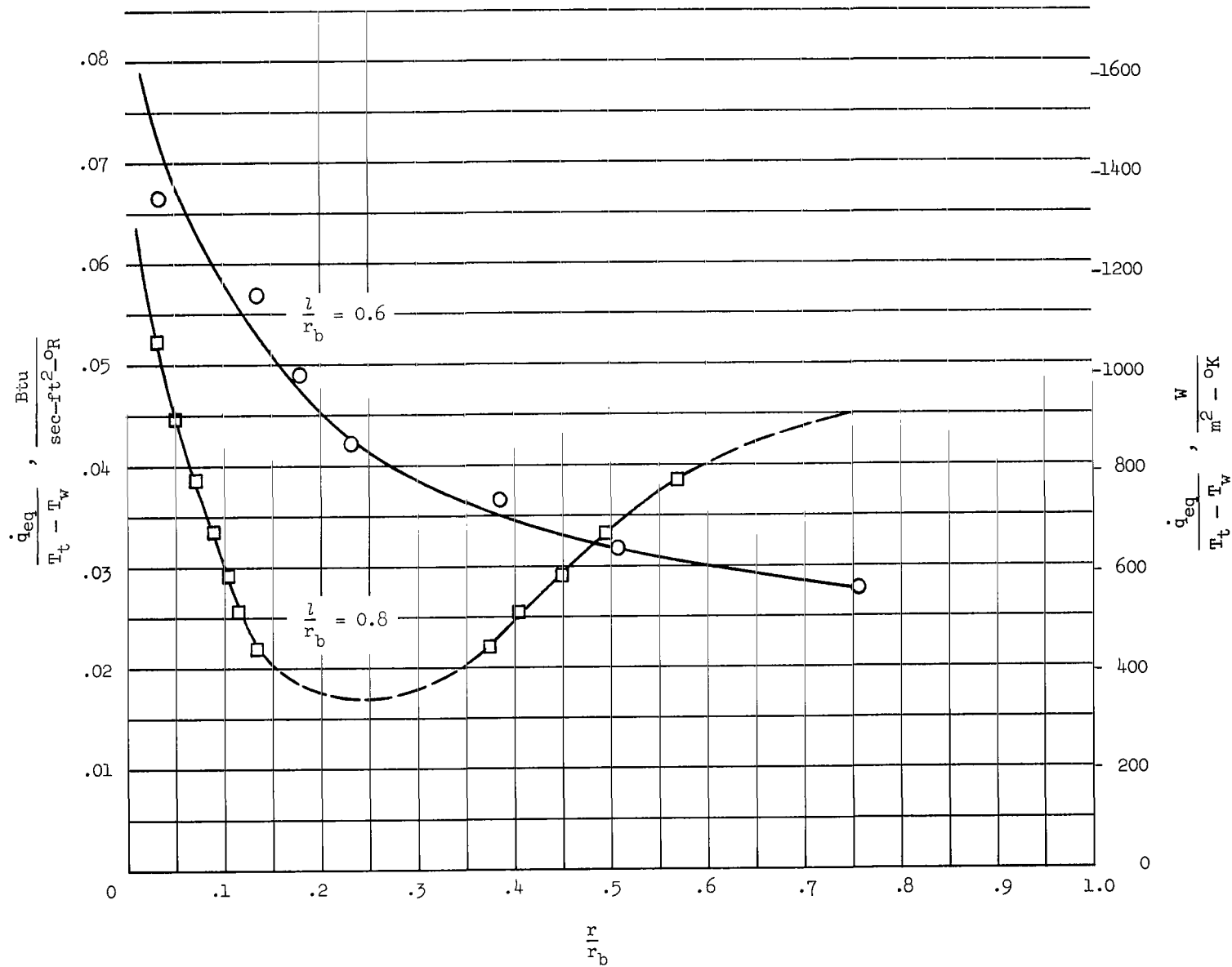
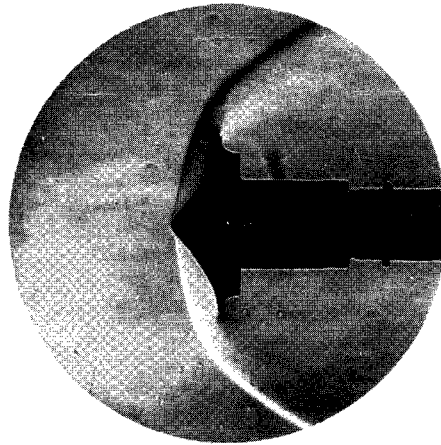


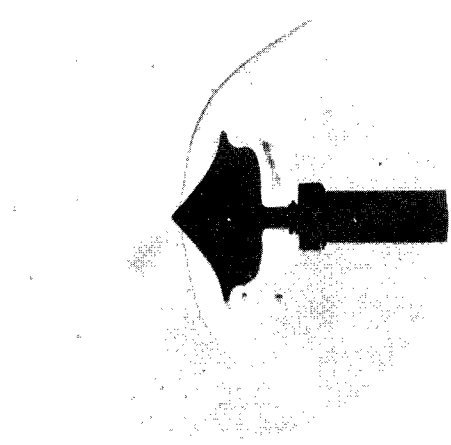
Figure 17.- Comparison of radiation-equilibrium heating distributions of models with  $l/r_b = 0.6$  and  $0.8$ .  $\alpha = 0^\circ$ ;  $R_H/r_b = 0$ ;  $R_D = 0.09 \times 10^6$ .



Aerodynamic – force  
model



Pressure – distribution  
model

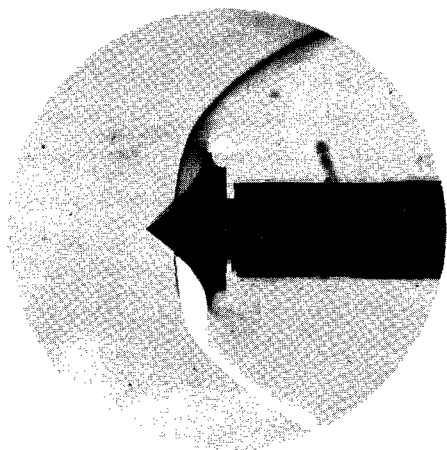


Heating – distribution  
model

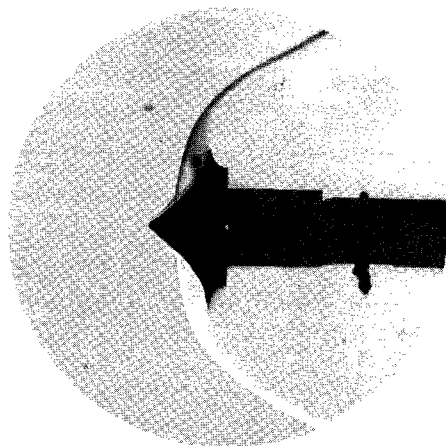
(a)  $z/r_b = 0.6$ ;  $R_D = 0.09 \times 10^6$ .

L-65-152

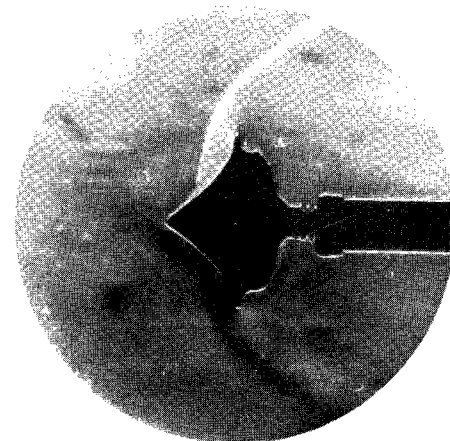
Figure 18.- Comparison of flow fields about the force, pressure, and heating models with  $z/r_b$  values of 0.6 and 0.8.  $\alpha = 0^\circ$ ;  $R_n/r_b = 0$ ;  $R_D = 0.09 \times 10^6$  and  $0.13 \times 10^6$ .



Aerodynamic-force  
model



Pressure-distribution  
model



Heating-distribution  
model

(b)  $l/r_b = 0.8$ ;  $R_D = 0.13 \times 10^6$ .

Figure 18.- Concluded.

L-65-153

3/18/85  
07

*"The aeronautical and space activities of the United States shall be conducted so as to contribute . . . to the expansion of human knowledge of phenomena in the atmosphere and space. The Administration shall provide for the widest practicable and appropriate dissemination of information concerning its activities and the results thereof."*

—NATIONAL AERONAUTICS AND SPACE ACT OF 1958

## NASA SCIENTIFIC AND TECHNICAL PUBLICATIONS

**TECHNICAL REPORTS:** Scientific and technical information considered important, complete, and a lasting contribution to existing knowledge.

**TECHNICAL NOTES:** Information less broad in scope but nevertheless of importance as a contribution to existing knowledge.

**TECHNICAL MEMORANDUMS:** Information receiving limited distribution because of preliminary data, security classification, or other reasons.

**CONTRACTOR REPORTS:** Technical information generated in connection with a NASA contract or grant and released under NASA auspices.

**TECHNICAL TRANSLATIONS:** Information published in a foreign language considered to merit NASA distribution in English.

**TECHNICAL REPRINTS:** Information derived from NASA activities and initially published in the form of journal articles.

**SPECIAL PUBLICATIONS:** Information derived from or of value to NASA activities but not necessarily reporting the results of individual NASA-programmed scientific efforts. Publications include conference proceedings, monographs, data compilations, handbooks, sourcebooks, and special bibliographies.

*Details on the availability of these publications may be obtained from:*

SCIENTIFIC AND TECHNICAL INFORMATION DIVISION  
NATIONAL AERONAUTICS AND SPACE ADMINISTRATION  
Washington, D.C. 20546